

Investigating amorphization as a deformation mechanism using a novel phase field model at the mesoscale

Yuntong Huang^a, Shuyang Dai^{b,*}, Chuqi Chen^a, Yang Xiang^{a,c,*}

^a*Department of Mathematics, The Hong Kong University of Science and Technology, Hong Kong, China*

^b*School of Mathematics and Statistics, Wuhan University, Wuhan, Hubei, China*

^c*HKUST Shenzhen-Hong Kong Collaborative Innovation Research Institute, Futian, Shenzhen, China*

Abstract

Amorphization during severe plastic deformation has been observed in various crystalline materials, yet its underlying mechanisms remain poorly understood. This study introduces a novel phase-field model at the mesoscale, integrating elastoplastic theory with a deviatoric stress-dependent transformation strain tensor to capture stress-induced amorphization. The model enables quantitative predictions of amorphous phase nucleation and propagation under high stress, resolving distinctive microstructural patterns such as amorphous shear bands. Simulations reveal key phenomena, including avalanche-like amorphization, grain size effects, the Hall-Petch effect, and surface amorphization, consistent with experimental observations. By bridging phase-field methods with elastoplastic theory, this work provides a robust framework for studying amorphization as a deformation mechanism and offers valuable insights for designing materials resistant to extreme mechanical conditions.

Keywords: amorphization, phase field model, finite deformation theory, transformation strain, Hall-Petch effect

1. Introduction

Amorphization under severe plastic deformation has been widely reported in crystalline materials, including alloys, ceramics, and metallic glasses [1–15]. Two primary mechanisms have been proposed for this solid phase transition: strain-induced amorphization and stress-induced amorphization [1, 12, 16–19]. Strain-induced amorphization is attributed to the progressive accumulation of defects, such as dislocations and grain boundaries, which destabilize the crystalline structure over time [1, 16]. In contrast, stress-induced amorphization involves the direct nucleation of amorphous phases under high stress, often in the absence of significant defect activities, and is triggered by

Email addresses: shuyang_dai@whu.edu.cn (Shuyang Dai), maxiang@ust.hk (Yang Xiang)

*Corresponding authors.

elastic instability or localized stress concentrations [12, 20–22]. For example, stress-induced amor-
10 phization at grain boundaries, without dislocation activity, challenges strain-centric theories [23].
Similarly, in situ deformation experiments have revealed the formation of amorphous shear bands
in highly stressed regions, further supporting the stress-driven mechanism [21]. This work focuses
on stress-induced amorphization to investigate its role in the deformation behavior of crystalline
materials and to provide new insights into the underlying mechanisms governing this transition.

Molecular dynamics (MD) simulations have provided atomic-scale insights into amorphization,
such as simulations on nanoindentation [24] and shear deformation [13], revealing grain boundaries
as nucleation sites [14]. However, MD simulations are limited by their reliance on picosecond-scale
timescales and nanometer-scale domains, which restrict their ability to capture macroscale plasticity
or experimentally relevant strain rates. In contrast, phase field (PF) modeling offers a mesoscale
20 framework capable of simulating microstructure evolution driven by thermodynamic forces and has
been successfully applied in martensitic transformation, deformation twinning, fracture, et al. [25–
56]. Phase field theory holds promise for investigating deformation-induced amorphization [57–60].
For instance, Clayton et al. [59] proposed a phase field model of pressure-induced amorphization
in boron carbide ceramic, incorporating elastic instability as a trigger to amorphization. However,
existing PF models neglect critical aspects of stress-induced amorphization, such as the coupling
between severe plastic deformation and phase transformation, and the special transformation strain
for amorphization. Notably, PF studies incorporating finite-strain theory provide a robust frame-
work for studying multiphase problems under severe plastic deformation [35, 50, 61–64]. What is
more, new transformation strains, which break from classical crystallographic definitions but are
30 thermodynamically consistent, are also developed [65]. Considering these advancements on PF
modeling, PF approaches can overcome the limitations of MD simulation and uncover the defor-
mation mechanisms governing the formation and behavior of amorphous phases in large-deformed
crystalline materials. This makes PF modeling a promising tool for studying deformation-induced
amorphization.

We propose a novel phase field model that couples elastoplasticity with phase transformation
to study stress-induced amorphization. The local crystallinity is described by a phase variable,
which evolves under a driving force derived from strain energy. Building on the work of Levitas
and Samani [65] and Gao [66], our model introduces a deviatoric stress-dependent transformation
strain. Specifically, the volumetric strain is governed by the density ratio of amorphous and crys-
40 talline phases, while the deviatoric strain is proportional to the applied deviatoric stress, departing
from crystallographic definitions (e.g., for martensite and twins). Thermodynamics consistency for

the kinetic equations is also guaranteed by the Clausius-Duhem inequality [65]. The model couples plasticity in both phases through stored elastic strain energy, enabling the simulation of defect evolution, such as shear bands and dislocations, during amorphization. By combining transformation strain energy and plastic work, the severely deformed materials overcome the energy barrier of amorphization in the model. The proposed framework for studying stress-induced amorphization at the continuum scale allows for quantitative investigations of microstructural evolution and offers new insights into the mechanisms driving amorphization under severe deformation.

We investigate key phenomena in stress-induced amorphization, including amorphous shear bands, grain size effect, and surface amorphization. Simulations reveal the formation and propagation of amorphous shear bands under severe deformation, driven by the elastic instability in crystalline phases, consistent with experimental observation [14, 15, 18, 67, 68]. Grain size effects are also captured, showing that smaller grains facilitate amorphization, while larger grains increase the difficulty of forming amorphous phases, aligning with experimental findings [13, 15, 24, 69]. A novel discovery is the critical-like behavior of stress-induced amorphization, characterized by avalanche dynamics associated with the formation of amorphous shear bands. This behavior, observed for the first time, highlights the relationship between amorphization and plasticity. Additionally, the simulations reproduce the classic Hall-Petch effect, where smaller grains lead to higher yield stress, further validating the ability of the proposed model to capture fundamental material behaviors [69]. Finally, three-dimensional compression simulations demonstrate that amorphous phases nucleate at surfaces and stress concentrators, consistent with in situ TEM studies [6, 9, 11, 13, 15]. These findings underscore the ability of the proposed model to quantitatively investigate the essential features of stress-induced amorphization.

The paper is structured as follows: Section 2 introduces the phase field model for amorphization, incorporating finite-strain elastoplasticity to capture the coupling between stress and phase transformation. Section 3 develops a linearized theory to improve computational efficiency, enabling faster simulations without compromising accuracy. Section 4 applies the model to 2D and 3D scenarios, providing insights into amorphous shear bands, grain size effects, and surface amorphization. Finally, Section 5 concludes the study by summarizing key findings and discussing future directions for extending the model to more complex deformation mechanisms.

2. Phase field model for amorphization

This section presents the phase field model coupled with finite strain theory to study stress-induced amorphization. The model is developed under the assumption of an isothermal system,

which simplifies the analysis by neglecting the effects of thermal loads associated with the two phases. This assumption allows us to focus on the mechanical and structural aspects of amorphization.

To describe the kinematics of finite deformation, we consider a reference configuration $\Omega_0 \subset \mathbb{R}^3$ and a material point \mathbf{x} within Ω_0 . The deformation is represented by a mapping $\mathcal{X}(\mathbf{x}) : \mathbf{x} \in \Omega_0 \rightarrow \mathbf{X} \in \Omega$, which maps the material point \mathbf{x} in the reference configuration to its position \mathbf{X} in the deformed configuration Ω . The deformation gradient, referred to the undeformed configuration, is denoted by $\mathbf{F} = \frac{\partial \mathcal{X}}{\partial \mathbf{x}}$. This mathematical framework provides the foundation for modeling the coupling between stress and phase transformation during amorphization.

2.1. Order parameters

We define a continuous field variable, $\eta \in [0, 1]$, to describe the crystallinity of materials. Specifically, $\eta = 0$ represents the crystalline phase, while $\eta = 1$ corresponds to the amorphous phase. The amorphous volume fraction, V_g , is described by the interpolation function:

$$V_g = h(\eta) = 2\eta^2 - \eta^4, \quad (1)$$

which ensures smooth transitions between phases. The derivatives of $h(\eta)$ vanish at $\eta = 0$ and $\eta = 1$, ensuring stability at the pure crystalline and amorphous states. This specific form of $h(\eta)$ is chosen for its simplicity and ability to capture the nonlinear evolution of the amorphous phase.

To account for the mass density of materials, we denote ρ_c and ρ_g as the mass densities of the crystalline and amorphous phases, respectively. The overall mass density of the system is expressed using the standard rule of mixtures [60]:

$$\rho = (1 - V_g)\rho_c + V_g\rho_g. \quad (2)$$

This formulation provides a consistent framework for linking the phase variable η to the physical properties, enabling the study of stress-induced amorphization.

2.2. Kinematics

The assumption of equal deformation gradients between the crystalline and amorphous phases is commonly used in multiphase modeling [60]. This assumption simplifies the analysis by ensuring consistency in the mechanical response of the two phases. Specifically, we assume that the deformation gradients of the crystalline and amorphous phases are identical, leading to the following equality (Figure 1) [44, 64],

$$\mathbf{F} = \mathbf{F}_c = \mathbf{F}_g, \quad (3)$$

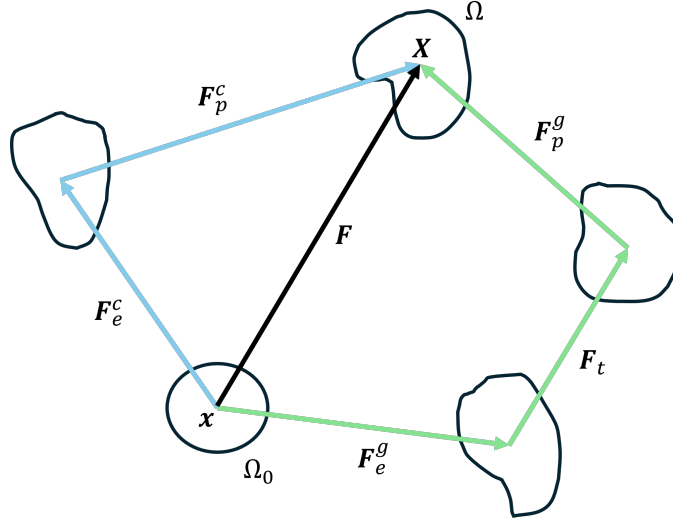


Figure 1: The decomposition of the deformation gradient for each phase. For the crystalline phase, the deformation gradient is expressed as $\mathbf{F}_c = \mathbf{F}_e^c \mathbf{F}_p^c$, where \mathbf{F}_e^c and \mathbf{F}_p^c denote the elastic and plastic components, respectively. In contrast, the deformation gradient for the amorphous phase is given by $\mathbf{F}_g = \mathbf{F}_e^g \mathbf{F}_t \mathbf{F}_p^g$, where \mathbf{F}_t accounts for the transformation strain during amorphization. \mathbf{F}_e^g and \mathbf{F}_p^g represent the elastic and plastic components of the amorphous phase, respectively.

where \mathbf{F}_c and \mathbf{F}_g are the deformation gradients of the crystalline and amorphous phases, respectively.

Figure 1 illustrates the decomposition of the deformation gradient for each phase, which provides a consistent framework for modeling the mechanical contributions of both phases during stress-induced amorphization.

For crystalline phases, the deformation gradient is multiplicatively decomposed into elastic and plastic components as,

$$\mathbf{F}_c = \mathbf{F}_e^c \mathbf{F}_p^c, \quad (4)$$

where \mathbf{F}_e^c represents the elastic deformation gradient, and \mathbf{F}_p^c accounts for the inelastic part of deformation gradient. The evolution of the plastic deformation gradient is governed by:

$$\dot{\mathbf{F}}_p^c = \mathbf{L}_p^c \mathbf{F}_p^c, \quad (5)$$

110 where \mathbf{L}_p^c is the plastic velocity gradient.

The plastic velocity gradient is expressed as the sum of the shear rates on N_s slip systems [35, 46, 63, 70, 71]:

$$\mathbf{L}_p^c = \sum_{\alpha=1}^{N_s} \dot{\gamma}^\alpha \mathbf{m}^\alpha \otimes \mathbf{n}^\alpha, \quad (6)$$

where $\dot{\gamma}^\alpha$ is the shear rate on the slip system α , and the vectors \mathbf{m}^α and \mathbf{n}^α are the slip direction and slip plane normal, respectively.

An isotropic plastic flow rule is assumed for the crystalline phases. The shear rate on slip system α is given by [62, 71]:

$$\dot{\gamma}^\alpha = \dot{\gamma}_0 \left| \frac{\tau^\alpha}{\tau_c^\alpha} \right|^{\frac{1}{m}} \text{sign}(\tau^\alpha), \quad (7)$$

where τ^α is the resolved shear stress, τ_c^α is the slip resistance, $\dot{\gamma}_0$ is the reference shear rate, and m is the strain rate sensitivity. The slip resistance evolves according to the hardening behavior:

$$\tau_c^\alpha = \sum_{\beta=1}^{N_s} h_{\alpha\beta} |\dot{\gamma}^\beta|, \quad (8)$$

where $h_{\alpha\beta}$ is the hardening matrix, and β indexes the slip systems.

120 For the amorphous phase, the deformation gradient is decomposed as,

$$\mathbf{F}_g = \mathbf{F}_e^g \mathbf{F}_t \mathbf{F}_p^g, \quad (9)$$

where \mathbf{F}_e^g denotes the elastic deformation gradient. \mathbf{F}_t is the transformation deformation gradient, and \mathbf{F}_p^g represents the plastic deformation gradient. The plastic behavior of amorphous phases is governed by the evolution of the plastic deformation gradient,

$$\dot{\mathbf{F}}_p^g = \mathbf{L}_p^g \mathbf{F}_p^g, \quad (10)$$

where the plastic velocity gradient is expressed as [66, 72, 73],

$$\mathbf{L}_p^g = \dot{\gamma}_g (\mathbf{R}_e^g)^T \mathbf{N} \mathbf{R}_e^g, \quad (11)$$

with $\mathbf{R}_e^g = \mathbf{F}_e^g [(\mathbf{F}_e^g)^T \mathbf{F}_e^g]^{-\frac{1}{2}}$ as the elastic rotation tensor and \mathbf{N} as the visco-plastic flow vector:

$$\mathbf{N} = \sqrt{\frac{1}{2}} \frac{\hat{\boldsymbol{\tau}}^g}{\|\hat{\boldsymbol{\tau}}^g\|}, \quad (12)$$

where $\hat{\boldsymbol{\tau}}^g$ as the deviatoric second Kirchhoff stress tensor and $\|\cdot\|$ denotes the Frobenius norm. The visco-plastic multiplier $\dot{\gamma}_g$ is given by,

$$\dot{\gamma}_g = \frac{1}{A} \sinh \frac{\hat{\tau}_{eq}^g}{\tau^*}, \quad (13)$$

where $\hat{\tau}_{eq}^g = \sqrt{\frac{1}{2}} \|\hat{\boldsymbol{\tau}}^g\|$ is the equivalent Kirchhoff stress tensor, $\tau^* = \frac{2k_B T}{V_{\text{atom}}}$ is the reference stress, and A is a material parameter. V_{atom} is the atomic volume, k_B is the Boltzmann constant and T is the absolute temperature.

130

As a summary, the plastic deformation in amorphous phases evolves as follows:

$$\mathbf{L}_p^g = \frac{1}{A} \sinh \frac{\hat{\tau}_{eq}^g}{\tau^*} (\mathbf{R}_e^g)^T \mathbf{N} \mathbf{R}_e^g. \quad (14)$$

Inspired by Levitas and Samani [65] and the creep behavior of amorphous materials [72], we introduce a novel transformation strain tensor to describe amorphization. Unlike martensitic transformations, this transformation strain is not determined by crystallography but is governed by a thermodynamically consistent kinetic equation. The transformation strain is decomposed as,

$$\mathbf{F}_t = \frac{1}{3}\varepsilon_0\mathbf{I} + \mathbf{F}_t^d, \quad (15)$$

where ε_0 represents volumetric strain due to change in mass density between the crystalline and amorphous phases, and \mathbf{F}_t^d is the deviatoric part of the transformation strain. The evolution of \mathbf{F}_t^d is governed by:

$$\dot{\mathbf{F}}_t^d = \mathbf{L}_t\mathbf{F}_t^d, \quad (16)$$

where the velocity gradient \mathbf{L}_t is formulated as:

$$\begin{aligned} \mathbf{L}_t &= \eta(1 - \eta)\dot{\eta}\text{sign}(\dot{\eta})\dot{\gamma}_t \sinh \frac{\hat{\tau}_{eq}^g}{\tau^*}(\mathbf{R}_e)^T \mathbf{N} \mathbf{R}_e \\ &= \sqrt{\frac{1}{2}}\eta(1 - \eta)\dot{\eta}\text{sign}(\dot{\eta})\dot{\gamma}_t \sinh \frac{\hat{\tau}_{eq}^g}{\tau^*}(\mathbf{R}_e)^T \frac{\hat{\boldsymbol{\tau}}^g}{\|\hat{\boldsymbol{\tau}}^g\|} \mathbf{R}_e, \end{aligned} \quad (17)$$

140 which $\dot{\gamma}_t$ is the shear rate for amorphization. In the next section, we will derive the work-conjugate force of the transformation strain, which is the second Piola-Kirchhoff stress, using the second law of thermodynamics. Then, we combine this thermodynamic consistency requirement and the creep behavior of amorphous phases to define the new transformation strain and hence $\sinh \frac{\hat{\tau}_{eq}^g}{\tau^*}(\mathbf{R}_e)^T \mathbf{N} \mathbf{R}_e$ is introduced. Furthermore, the introduction of $\eta(1 - \eta)\dot{\eta}\text{sign}(\dot{\eta})$ ensures that the transformation strain evolves only during phase transitions, maintaining stability in pure crystalline and amorphous states.

2.3. Free energy functional

The specific (per mass) free energy functional of the system, ψ , governs the evolution of the material system and consists of three main components: the local phase separation energy ψ^{ch} , the 150 gradient energy ψ^∇ , and the elastic strain energy in crystalline and amorphous phases, ψ_e^c and ψ_e^g , respectively. The free energy functional density is expressed as:

$$\begin{aligned} \psi(\eta, \mathbf{F}_e^c, \mathbf{F}_e^g, \nabla\eta) &= (1 - h(\eta))\psi_e^c(\mathbf{F}_e^c) + h(\eta)J_g\psi_e^g(\mathbf{F}_e^g(\eta)) \\ &+ \psi^{ch}(\eta) + \psi^\nabla(\nabla\eta), \end{aligned} \quad (18)$$

where η is the order parameter describing the crystallinity of the material, and $h(\eta)$ represents the local volume fraction of the amorphous phase. The term ψ^{ch} captures the bulk thermodynamic properties of the system, ψ^∇ accounts for the interfacial energy between phases, and ψ_e^c and ψ_e^g represent the elastic strain energy densities in the crystalline and amorphous phases, respectively.

This free energy functional provides a comprehensive framework for modeling the interplay between phase separation, interfacial effects, and mechanical deformation, which are critical for understanding stress-induced amorphization.

2.3.1. Local phase separation energy

160 The local phase separation energy density, ψ^{ch} , captures the bulk thermodynamic properties of the system and is represented by a Landau-type polynomial:

$$\psi^{ch}(\eta) = \kappa \left(\frac{A}{2}\eta^2 - \frac{B}{3}\eta^3 + \frac{C}{4}\eta^4 \right), \quad (19)$$

where the parameter κ represents the energy difference between the crystalline and amorphous phases. The constants A , B , and C determine the shape of the local phase separation energy.

To ensure thermodynamic consistency, the free energy of the amorphous phase must be higher than that of the crystalline phase, i.e., $\psi^{ch}(0) = 0$, [14]. This requirement imposes the following constraint:

$$\frac{A}{2} - \frac{B}{3} + \frac{C}{4} > 0. \quad (20)$$

Additionally, the partial derivative of ψ^{ch} with respect to η must vanish at $\eta = 0$ and $\eta = 1$, ensuring that the pure crystalline and amorphous phases correspond to local energy minima. The condition leads to the constraints:

$$A - B + C = 0. \quad (21)$$

170 These constraints guide the selection of suitable parameters for numerical simulations, ensuring that the energy landscape is physically meaningful.

The driving force associated with the local phase separation energy is given by the derivative of ψ^{ch} with respect to η :

$$\frac{\partial \psi^{ch}}{\partial \eta} = \kappa (A\eta - B\eta^2 + C\eta^3). \quad (22)$$

2.3.2. Gradient energy

The gradient energy represents the energy associated with the interface between two phases, capturing the cost of maintaining a spatially varying phase field. Its density, ψ^∇ , is expressed as:

$$\psi^\nabla(\nabla\eta) = \frac{1}{2}\beta|\nabla\eta|^2, \quad (23)$$

where β is a coefficient related to the interfacial energy between the crystalline and amorphous phases. This term ensures a smooth transition between phases by penalizing sharp gradients in the phase field variable η .

The driving force associated with the gradient energy is derived from its functional derivative with respect to $\nabla\eta$ and is given by,

$$\nabla \frac{\partial \psi^\nabla}{\partial \nabla \eta} = \beta \nabla^2 \eta. \quad (24)$$

This expression will be used in the Clausius-Duhem inequality to derive the kinetic equations governing the evolution of the phase field variable η .

2.3.3. Strain energy

The elastic strain energy density in the crystalline phase, ψ_e^c , quantifies the stored energy due to elastic deformation and can be written as,

$$\psi_e^c(\mathbf{F}_e^c) = \frac{1}{2} \mathbf{E}_e^c : \mathbb{C}_c : \mathbf{E}_e^c, \quad (25)$$

where $\mathbf{E}_e^c = \frac{1}{2} ((\mathbf{F}_e^c)^T \mathbf{F}_e^c - I)$ is the elastic strain tensor, and \mathbb{C}_c represents the elastic stiffness tensor for the crystalline phase.

The stress tensors associated with the elastic strain energy are derived as follows. The first Piola-Kirchhoff stress tensor, $\mathbf{P}^c = \rho_c \frac{\partial \psi_e^c}{\partial \mathbf{F}_e^c}$, i.e.,

$$\mathbf{P}^c = \rho_c \mathbf{F}_e^c \cdot \frac{\partial \psi_e^c}{\partial \mathbf{E}_e^c} \cdot (\mathbf{F}_e^c)^{-1}, \quad (26)$$

where ρ_c is the mass density in crystalline domain, assumed to remain constant during deformation.

The Cauchy stress tensor, $\boldsymbol{\sigma}^c$, and the second Piola-Kirchhoff stress tensor $\hat{\boldsymbol{\sigma}}^c$ are expressed as,

$$\boldsymbol{\sigma}^c = \rho_c \mathbf{F}_e^c \cdot \frac{\partial \psi_e^c}{\partial \mathbf{E}_e^c} \cdot (\mathbf{F}_e^c)^T, \quad (27)$$

$$\hat{\boldsymbol{\sigma}}^c = \rho_c \frac{\partial \psi_e^c}{\partial \mathbf{E}_e^c}. \quad (28)$$

These stress tensors are related through the following identities:

$$\begin{aligned} \mathbf{P}^c &= \mathbf{F}_e^c \cdot \hat{\boldsymbol{\sigma}}^c \cdot (\mathbf{F}_e^c)^{-1}, \\ \boldsymbol{\sigma}^c &= \mathbf{F}_e^c \cdot \hat{\boldsymbol{\sigma}}^c \cdot (\mathbf{F}_e^c)^T, \\ \rho_c \frac{\partial \psi_e^c}{\partial \mathbf{F}_e^c} &= \hat{\boldsymbol{\sigma}}^c \cdot \mathbf{F}_e^c. \end{aligned}$$

For the amorphous phase, the elastic strain energy density, ψ_e^g , is expressed as:

$$\psi_e^g(\mathbf{F}_e^g(\eta)) = \frac{1}{2} \mathbf{E}_e^g : \mathbb{C}_g : \mathbf{E}_e^g, \quad (29)$$

where $\mathbf{E}_e^g = \frac{1}{2} ((\mathbf{F}_e^g)^T \mathbf{F}_e^g - I)$ is the elastic strain tensor, and \mathbb{C}_g represents the elastic coefficient tensor for the amorphous phase. The elastic deformation gradient $\mathbf{F}_e^g(\eta) = (\mathbf{F}_t(\eta) \mathbf{F}_p^g)^{-1} \mathbf{F}$ depends on the phase field variable η due to the transformation strain \mathbf{F}_t . Similar to the crystalline phase, the

first Piola-Kirchhoff stress tensor \mathbf{P}^g , the Cauchy stress tensor $\boldsymbol{\sigma}^g$, and the second Piola-Kirchhoff stress tensor $\hat{\boldsymbol{\sigma}}^g$ with respect to the unloaded configuration Ω_0 are given by,

$$\begin{aligned}\mathbf{P}^g &= \rho_g \mathbf{F}_e^g \cdot \frac{\partial \psi_e^g}{\partial \mathbf{E}_e^g} \cdot (\mathbf{F}_t \mathbf{F}_p^g)^{-1}, \\ \boldsymbol{\sigma}^g &= \rho_g \mathbf{F}_e^g \cdot \frac{\partial \psi_e^g}{\partial \mathbf{E}_e^g} \cdot (\mathbf{F}_e^g)^T, \\ \hat{\boldsymbol{\sigma}}^g &= \rho_g \frac{\partial \psi_e^g}{\partial \mathbf{E}_e^g},\end{aligned}\tag{30}$$

200 where the density of the amorphous phase ρ_g is also assumed to remain constant during deformation. We also find the following equations relating stress tensors

$$\begin{aligned}\mathbf{P}^g &= \mathbf{F}_e^g \cdot \hat{\boldsymbol{\sigma}}^g \cdot (\mathbf{F}_t \mathbf{F}_p^g)^{-1}, \\ \boldsymbol{\sigma}^g &= \mathbf{F}_e^g \cdot \hat{\boldsymbol{\sigma}}^g \cdot (\mathbf{F}_e^g)^T, \\ \rho_g \frac{\partial \psi_e^g}{\partial \mathbf{F}_e^g} &= \hat{\boldsymbol{\sigma}}^g \cdot \mathbf{F}_e^g.\end{aligned}$$

The driving force associated with the elastic strain energy will be derived from the Clausius-Duhem inequality later.

2.3.4. Balance laws

During deformation, the local form of the linear momentum balance governs the mechanical equilibrium of the system and is expressed as::

$$\nabla \cdot \mathbf{P} = 0,\tag{31}$$

where \mathbf{P} is the first Piola-Kirchhoff stress tensor. This equation ensures that the internal and external forces are balanced at every material point, providing a fundamental framework for describing deformation behavior.

210 To model isothermal and irreversible deformation processes, it is essential to formulate constitutive relations that are thermodynamically consistent. This ensures that the model adheres to the second law of thermodynamics and accurately captures the energy dissipation associated with deformation. The next section discusses the thermodynamic formalism required to derive these constitutive relations and their role in the phase field model for stress-induced amorphization.

2.3.5. Second law of thermodynamics

The second law of thermodynamics provides a rigorous framework for deriving the driving forces governing the evolution of strains and amorphization. Under isothermal conditions, the Clausius-Duhem inequality is written per unit reference volume as [25, 29, 61, 74, 75],

$$\int_{\Omega_0} \mathbf{P} : \dot{\mathbf{F}} - \rho_c \dot{\psi} d\Omega_0 \geq 0,\tag{32}$$

where \mathbf{P} is the first Piola-Kirchhoff stress tensor, \mathbf{F} is the deformation gradient, and ψ is the free energy density. The inequality ensures that the rate of energy dissipation is non-negative.

The rates of total deformation $\dot{\mathbf{F}}$ and free energy density $\dot{\psi}$ are given by:

$$\dot{\mathbf{F}} = \dot{\mathbf{F}}_e^c \mathbf{F}_p^c + \mathbf{F}_e^c \dot{\mathbf{F}}_p^c, \quad (33)$$

$$\begin{aligned} \dot{\psi} = & (1 - h(\eta)) \frac{\partial \psi_e^c}{\partial \mathbf{F}_e^c} : \dot{\mathbf{F}}_e^c + h(\eta) J_g \frac{\partial \psi_e^g}{\partial \mathbf{F}_e^g} : \dot{\mathbf{F}}_e^g + \frac{\partial \psi^\nabla}{\partial \nabla \eta} \cdot \dot{\nabla} \eta \\ & + \left[(J_g \psi_e^g - \psi_e^c) h'(\eta) + h(\eta) \rho_g \frac{\partial \psi_e^g}{\partial \eta} + \frac{\partial \psi^{ch}}{\partial \eta} \right] \dot{\eta}, \end{aligned} \quad (34)$$

which can be obtained from Equation 4 and 18.

Substituting these expressions into the Clausius-Duhem inequality leads to:

$$\begin{aligned} & \int_{\Omega_0} \left[\mathbf{F}_p^c \cdot \mathbf{P} - (1 - h(\eta)) \rho_c \frac{\partial \psi_e^c}{\partial \mathbf{F}_e^c} - h(\eta) \rho_g \mathbf{F}_p^c \cdot (\mathbf{F}_t \cdot \mathbf{F}_p^g)^{-1} \cdot \frac{\partial \psi_e^g}{\partial \mathbf{F}_e^g} \right] : \dot{\mathbf{F}}_e^c \\ & + \left[\mathbf{P} - h(\eta) \rho_g (\mathbf{F}_t \cdot \mathbf{F}_p^g)^{-1} \cdot \frac{\partial \psi_e^g}{\partial \mathbf{F}_e^g} \right] : \mathbf{F}_e^c \cdot \dot{\mathbf{F}}_p^c \\ & + h(\eta) \rho_g \mathbf{F}_p^g \cdot (\mathbf{F}_t \cdot \mathbf{F}_p^g)^{-1} \cdot \frac{\partial \psi_e^g}{\partial \mathbf{F}_e^g} : \mathbf{F}_e^g \cdot \dot{\mathbf{F}}_t \\ & + h(\eta) \rho_g (\mathbf{F}_t \cdot \mathbf{F}_p^g)^{-1} \cdot \frac{\partial \psi_e^g}{\partial \mathbf{F}_e^g} : \mathbf{F}_e^g \cdot \mathbf{F}_t \cdot \dot{\mathbf{F}}_p^g \\ & - \rho_c \frac{\partial \psi^\nabla}{\partial \nabla \eta} \cdot \dot{\nabla} \eta - \left[(\rho_g \psi_e^g - \rho_c \psi_e^c) h'(\eta) + h(\eta) \rho_g \frac{\partial \psi_e^g}{\partial \eta} + \rho_c \frac{\partial \psi^{ch}}{\partial \eta} \right] \dot{\eta} d\Omega_0 \geq 0. \end{aligned} \quad (35)$$

The permutability of time and space differentiation in the reference configuration and the Gauss theorem are applied for the interfacial energy term,

$$\int_{\Omega_0} \frac{\partial \psi^\nabla}{\partial \nabla \eta} \cdot \dot{\nabla} \eta d\Omega_0 = - \int_{\Omega_0} \nabla \frac{\partial \psi^\nabla}{\partial \nabla \eta} \cdot \dot{\eta} d\Omega + \int_{\Sigma_0} \mathbf{n} \cdot \frac{\partial \psi^\nabla}{\partial \nabla \eta} \dot{\eta} d\Sigma_0, \quad (36)$$

where an additional boundary condition for phase transitions is assumed to cancel the surface dissipation,

$$\mathbf{n} \cdot \frac{\partial \psi^\nabla}{\partial \nabla \eta} = \beta \mathbf{n} \cdot \nabla \eta = 0. \quad (37)$$

Then, substituting Equation 36 into the Clausius-Duhem inequality, the dissipation rate becomes,

$$\begin{aligned} & \int_{\Omega_0} \left[\mathbf{F}_p^c \cdot \mathbf{P} - (1 - h(\eta)) \rho_c \frac{\partial \psi_e^c}{\partial \mathbf{F}_e^c} - h(\eta) \rho_g \mathbf{F}_p^c \cdot (\mathbf{F}_t \mathbf{F}_p^g)^{-1} \cdot \frac{\partial \psi_e^g}{\partial \mathbf{F}_e^g} \right] : \dot{\mathbf{F}}_e^c \\ & + \left[\mathbf{P} - h(\eta) \rho_g (\mathbf{F}_t \mathbf{F}_p^g)^{-1} \cdot \frac{\partial \psi_e^g}{\partial \mathbf{F}_e^g} \right] : \mathbf{F}_e^c \cdot \dot{\mathbf{F}}_p^c \\ & + h(\eta) \rho_g \mathbf{F}_p^g \cdot (\mathbf{F}_t \mathbf{F}_p^g)^{-1} \cdot \frac{\partial \psi_e^g}{\partial \mathbf{F}_e^g} : \mathbf{F}_e^g \cdot \dot{\mathbf{F}}_t \\ & + h(\eta) \rho_g (\mathbf{F}_t \mathbf{F}_p^g)^{-1} \cdot \frac{\partial \psi_e^g}{\partial \mathbf{F}_e^g} : \mathbf{F}_e^g \cdot \mathbf{F}_t \cdot \dot{\mathbf{F}}_p^g \\ & - \left[(\rho_g \psi_e^g - \rho_c \psi_e^c) h'(\eta) - \rho_c \nabla \frac{\partial \psi^\nabla}{\partial \nabla \eta} \right. \\ & \left. - h(\eta) \mathbf{F}_t^{-1} \boldsymbol{\sigma}^g : \frac{\partial \mathbf{F}_t}{\partial \eta} + \rho_c \frac{\partial \psi^{ch}}{\partial \eta} \right] \dot{\eta} d\Omega_0 \geq 0. \end{aligned} \quad (38)$$

Assuming that the rate of dissipation is independent of $\dot{\mathbf{F}}_e^c$, the constitutive relation for the first Piola-Kirchhoff stress tensor is deduced as:

$$\begin{aligned} \mathbf{P} &= (1 - h(\eta))\rho_c(\mathbf{F}_p^c)^{-1} \cdot \frac{\partial \psi_e^c}{\partial \mathbf{F}_e^c} - h(\eta)\rho_g(\mathbf{F}_t\mathbf{F}_p^g)^{-1} \cdot \frac{\partial \psi_e^g}{\partial \mathbf{F}_e^g} \\ &= (1 - h(\eta))\mathbf{P}^c + h(\eta)\mathbf{P}^g, \end{aligned} \quad (39)$$

where \mathbf{P}^c and \mathbf{P}^g , defined in Equation 26 and 30, are the stress tensors for the crystalline and amorphous phases, respectively.

The dissipation rate and driving forces for $\dot{\mathbf{F}}_p^c$, $\dot{\mathbf{F}}_t$, $\dot{\mathbf{F}}_p^g$, and $\dot{\eta}$ are given as,

$$\mathfrak{D} := \mathbf{X}_p^c : \dot{\mathbf{F}}_p^c + \mathbf{X}_t : \dot{\mathbf{F}}_t + \mathbf{X}_p^g : \dot{\mathbf{F}}_p^g + \dot{\mathbf{X}}_\eta \dot{\eta} \geq 0, \quad (40)$$

$$\mathbf{X}_p^c = (1 - h(\eta))\hat{\boldsymbol{\sigma}}^c \cdot (\mathbf{F}_p^c)^{-1}, \quad (41)$$

$$\mathbf{X}_t = h(\eta)\hat{\boldsymbol{\sigma}}^g \cdot (\mathbf{F}_t\mathbf{F}_p^g)^{-1}, \quad (42)$$

$$\mathbf{X}_p^g = h(\eta)\mathbf{F}_t^{-1} \cdot \hat{\boldsymbol{\sigma}}^g \cdot (\mathbf{F}_t\mathbf{F}_p^g)^{-1}, \quad (43)$$

$$\begin{aligned} \mathbf{X}_\eta &= - \left[(J_g\psi_e^g - \psi_e^c)h'(\eta) - \nabla \frac{\partial \psi^\nabla}{\partial \nabla \eta} + \frac{\partial \psi^{ch}}{\partial \eta} \right. \\ &\quad \left. - h(\eta)\mathbf{F}_t^{-1}\hat{\boldsymbol{\sigma}}^g : \frac{\partial \mathbf{F}_t}{\partial \eta} \right], \end{aligned} \quad (44)$$

where \mathbf{X}_p^c , \mathbf{X}_t , \mathbf{X}_p^g , and \mathbf{X}_η are work-conjugate driving forces for $\dot{\mathbf{F}}_p^c$, $\dot{\mathbf{F}}_t$, $\dot{\mathbf{F}}_p^g$, and $\dot{\eta}$, respectively. $\hat{\boldsymbol{\sigma}}^c$ and $\hat{\boldsymbol{\sigma}}^g$ are the elastic second Piola-Kirchhoff stress.

2.4. Kinetics equations

The evolution of the system is governed by the generalized rates of variables, which are functions of the work-conjugate driving forces. These rates are written as:

$$\mathbf{L}_p^c = f_p^c(\mathbf{X}_p^c, \eta), \mathbf{L}_t = f_t(\mathbf{X}_t, \eta), \mathbf{L}_p^g = f_p^g(\mathbf{X}_p^g, \eta), \dot{\eta} = f_\eta(\mathbf{X}_\eta, \eta). \quad (45)$$

Here, \mathbf{L}_p^c , \mathbf{L}_p^g , and \mathbf{L}_t are the plastic velocity gradients in the crystalline and amorphous phases and the transformational velocity gradient, respectively, as defined in Equation 6, 14 and 17. These definitions ensure thermodynamical consistency with the work-conjugate forces.

The evolution of the phase variable η is governed by the time-dependent Ginzburg-Landau (TDGL) equation, which assumes that the rate of change of field variables is proportional to the

thermodynamic driving force:

$$\dot{\eta} = M \left[-(\rho_g \psi_e^g - \rho_c \psi_e^c) h'(\eta) + \beta \nabla^2 \eta + h(\eta) \mathbf{F}_t^{-1} \boldsymbol{\sigma}^g : \frac{\partial \mathbf{F}_t}{\partial \eta} - \kappa (A\eta - B\eta^2 + C\eta^3) \right], \quad (46)$$

$$\mathbf{L}_p^c = \sum_{\alpha=1}^{N_s} \dot{\gamma}^\alpha \mathbf{m}^\alpha \times \mathbf{n}^\alpha, \quad (47)$$

$$\mathbf{L}_p^g = \frac{1}{A} \sinh \frac{\hat{\tau}_{eq}^g}{\tau^*} (\mathbf{R}_e)^T \mathbf{N} \mathbf{R}_e, \quad (48)$$

$$\mathbf{L}_t = \eta (1 - \eta) \dot{\eta} \text{sign}(\dot{\eta}) \dot{\gamma}_t \sinh \frac{\hat{\tau}_{eq}^g}{\tau^*} (\mathbf{R}_e)^T \mathbf{N} \mathbf{R}_e, \quad (49)$$

$$\mathbf{n} \cdot \nabla \eta = 0, \quad (50)$$

where the plastic velocity gradients in the crystalline and amorphous phases, as well as the transformational velocity gradient, are also given.

These evolution equations describe the coupled deformation and amorphization processes in the system. The TDGL equation governs the evolution of the phase field variable η , capturing the transition between crystalline and amorphous phases. The plastic velocity gradients \mathbf{L}_p^c and \mathbf{L}_p^g describe the plastic deformation in the crystalline and amorphous phases, while \mathbf{L}_t accounts for the transformation deformation gradient during amorphization. Together, these equations provide a comprehensive framework for modeling stress-induced amorphization and its interplay with plastic deformation.

3. Geometric linearization

The phase field model presented in the previous section incorporates finite strain theory to capture the coupling between stress and phase transformation during amorphization. While this framework provides a rigorous and comprehensive description of the deformation behavior, the nonlinear equations arising from finite strain mechanics significantly increase computational cost, making large-scale simulations time-consuming.

To address this challenge, we introduce a linearized theory based on linear elasticity. This simplification reduces computational complexity while retaining the essential physics of the model, enabling efficient simulations of stress-induced amorphization. By approximating the deformation behavior with linear elasticity, the model becomes more suitable for studying large-scale systems and exploring a wider range of material behaviors.

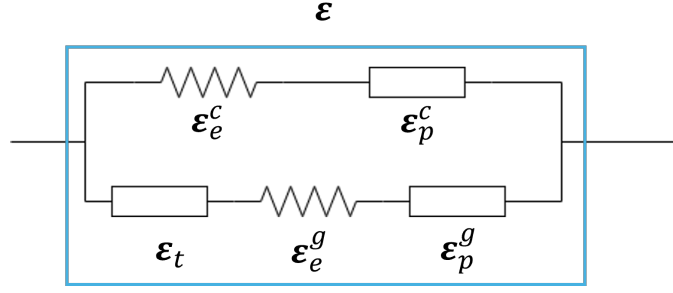


Figure 2: Schematic of the additive decomposition of the total strain for materials under deformation.

3.1. Kinematics

Under the assumption of linear elasticity, the total strain tensor of the system is written as,

$$\boldsymbol{\varepsilon} = \frac{1}{2}(\nabla \mathbf{u} + \nabla \mathbf{u}^T),$$

where \mathbf{u} is the displacement field during deformation. For simplicity, we assume that the total strain is equal in both crystalline and amorphous phases [60],

$$\boldsymbol{\varepsilon} = \boldsymbol{\varepsilon}_c = \boldsymbol{\varepsilon}_g, \quad (51)$$

where $\boldsymbol{\varepsilon}_c$ and $\boldsymbol{\varepsilon}_g$ are the total strain tensors in the crystalline and amorphous phases, respectively.

270 Figure 2 illustrates the additive decomposition of the total strain for material under deformation.

In the crystalline phase, an additive decomposition is assumed for the total strain tensor,

$$\boldsymbol{\varepsilon}_c = \boldsymbol{\varepsilon}_e^c + \boldsymbol{\varepsilon}_p^c,$$

where $\boldsymbol{\varepsilon}_e^c$ and $\boldsymbol{\varepsilon}_p^c$ represent the elastic and plastic strains, respectively. The elastic strain energy density in the crystalline phases, ψ_e^c , is given by:

$$\psi_e^c(\boldsymbol{\varepsilon}_e^c) = \frac{1}{2} \boldsymbol{\varepsilon}_e^c : \mathbb{C}_c : \boldsymbol{\varepsilon}_e^c, \quad (52)$$

where \mathbb{C}_c is the elastic stiffness tensor for the crystalline phase, and the stress tensor is, $\boldsymbol{\sigma}^c = \mathbb{C}_c : \boldsymbol{\varepsilon}_e^c$.

In the amorphous phase, the total strain tensor is decomposed into elastic, plastic, and transformation components:

$$\boldsymbol{\varepsilon}_g = \boldsymbol{\varepsilon}_e^g + \boldsymbol{\varepsilon}_t(\eta) + \boldsymbol{\varepsilon}_p^g, \quad (53)$$

where $\boldsymbol{\varepsilon}_e^g$, $\boldsymbol{\varepsilon}_t$, and $\boldsymbol{\varepsilon}_p^g$ represent the elastic strain, transformation strain, and plastic strain, respectively. The elastic strain energy density in the amorphous phase is:

$$\psi_e^g(\boldsymbol{\varepsilon}_e^g(\eta)) = \frac{1}{2} \boldsymbol{\varepsilon}_e^g : \mathbb{C}_g : \boldsymbol{\varepsilon}_e^g, \quad (54)$$

where \mathbb{C}_g is the elastic constant tensor of the amorphous phase, and $\boldsymbol{\sigma}^g = \mathbb{C}_g : \boldsymbol{\varepsilon}_e^g$ is the stress tensor.

280 The transformation strain $\boldsymbol{\varepsilon}_t$ accounts for the volumetric and deviatoric strain contributions during amorphization. It is defined as:

$$\boldsymbol{\varepsilon}_t = \frac{1}{3}\varepsilon_0\mathbf{I} + \mathbf{e}_t, \quad (55)$$

where ε_0 is the volumetric strain due to changes in mass density between the crystalline and amorphous phases, and \mathbf{e}_t is the deviatoric transformation strain. The evolution of \mathbf{e}_t is governed by:

$$\dot{\mathbf{e}}_t = \eta(1 - \eta)\dot{\eta}\text{sign}(\dot{\eta})\dot{\gamma}_t \sinh \frac{\sigma_e \mathbf{S}}{\sigma_c \sigma_e}, \quad (56)$$

where \mathbf{S} is the deviatoric stress tensor, i.e., $S_{ij} = \sigma_{ij} - \frac{1}{3}\sigma_{kk}\delta_{ij}$. Its J_2 invariant is the Mises stress, $\sigma_e = \sqrt{\frac{3}{2}\mathbf{S}^T\mathbf{S}}$. $\dot{\gamma}_t$ is the rate of transformation strain under stress. As previous discussion, the transformation strain ensures thermodynamic consistency and captures the stress-driven nature of amorphization, combining the creep behavior of the amorphous phase.

The plastic strain in the amorphous phase, $\boldsymbol{\varepsilon}_p^g$, follows a viscous flow model as [66, 72],

$$\dot{\boldsymbol{\varepsilon}}_p^g = \frac{1}{A} \sinh \frac{\sigma_e \mathbf{S}}{\tau^* \sigma_e}, \quad (57)$$

290 where A and τ^* are material constants, and σ_e is the equivalent stress. This model describes the time-dependent plastic deformation in the amorphous phase under linearized elasticity.

3.2. Thermodynamic laws

To derive the driving forces governing strains and amorphization, we begin by defining the specific (per mass) Helmholtz free energy functional as,

$$\begin{aligned} \psi(\eta, \nabla\eta, \boldsymbol{\varepsilon}_e^c, \boldsymbol{\varepsilon}_e^g) &= (1 - h(\eta))\psi_c^e(\boldsymbol{\varepsilon}_e^c) + h(\eta)J_g\psi_g^e(\boldsymbol{\varepsilon}_e^g(\eta)) \\ &+ \psi^{ch}(\eta) + \psi^\nabla(\nabla\eta), \end{aligned} \quad (58)$$

where $h(\eta)$ is the local volume fraction of the amorphous phase, and $J_g = \frac{\rho_g}{\rho_c}$ is the density ratio between the amorphous (ρ_g) and crystalline (ρ_c) phases.

Under isothermal conditions, the second law of thermodynamics is expressed in the form of the Clausius-Duhem inequality:

$$\rho_c \mathfrak{D} = \int_{\omega_0} \boldsymbol{\sigma} : \dot{\boldsymbol{\varepsilon}} - \rho_c \dot{\psi} d\Omega_0 \geq 0, \quad (59)$$

where \mathfrak{D} is the rate of dissipation per unit mass, $\boldsymbol{\sigma}$ is the Cauchy stress tensor, and $\dot{\psi}$ is the rate of change of the free energy density. Assuming constant densities ρ_c and ρ_g , the rate of free energy

300 density is given by,

$$\begin{aligned} \dot{\psi} = & (1 - h(\eta)) \frac{\partial \psi_c^e}{\partial \boldsymbol{\varepsilon}_e^c} : \dot{\boldsymbol{\varepsilon}}_e^c + h(\eta) J_g \frac{\partial \psi_g^e}{\partial \boldsymbol{\varepsilon}_e^g} : \dot{\boldsymbol{\varepsilon}}_e^g + (J_g \psi_e^g - \psi_e^c) h'(\eta) \dot{\eta} \\ & + h(\eta) J_g \frac{\partial \psi_e^g}{\partial \eta} \dot{\eta} + \frac{\partial \psi^{ch}}{\partial \eta} \dot{\eta} + \frac{\partial \psi^\nabla}{\partial \nabla \eta} \nabla \dot{\eta}. \end{aligned} \quad (60)$$

Substituting this expression into the Clausius-Duhem inequality and simplifying yields,

$$\begin{aligned} \int_{\Omega_0} \left\{ \boldsymbol{\sigma} - \left[(1 - h(\eta)) \rho_c \frac{\partial \psi_c^e}{\partial \boldsymbol{\varepsilon}_e^c} + h(\eta) \rho_g \frac{\partial \psi_g^e}{\partial \boldsymbol{\varepsilon}_e^g} \right] \right\} : \dot{\boldsymbol{\varepsilon}}_e^c + (\boldsymbol{\sigma} - h(\eta) \rho_g \frac{\partial \psi_g^e}{\partial \boldsymbol{\varepsilon}_p^c}) : \dot{\boldsymbol{\varepsilon}}_p^c \\ - h(\eta) \rho_g \frac{\partial \psi_g^e}{\partial \boldsymbol{\varepsilon}_p^g} : \dot{\boldsymbol{\varepsilon}}_p^g - h(\eta) \rho_g \frac{\partial \psi_g^e}{\partial \boldsymbol{\varepsilon}_t} : \dot{\boldsymbol{\varepsilon}}_t - \{ (\rho_g \psi_e^g - \rho_c \psi_e^c) h'(\eta) \\ - h(\eta) \rho_g \eta (1 - \eta) \dot{\gamma}_t \sinh \frac{\sigma_e}{\sigma_c} \boldsymbol{\sigma}^g : \frac{\mathbf{S}}{\sigma_e} \text{sign}(\dot{\eta}) + \rho_c \frac{\partial \psi^{ch}}{\partial \eta} - \rho_c \nabla \frac{\partial \psi^\nabla}{\partial \nabla \eta} \} \dot{\eta} d\Omega_0 \geq 0. \end{aligned} \quad (61)$$

Assuming that the rate of dissipation is independent of $\dot{\boldsymbol{\varepsilon}}_e^c$, the constitutive relation for the Cauchy stress tensor can be deduced as,

$$\boldsymbol{\sigma} = (1 - h(\eta)) \boldsymbol{\sigma}^c + h(\eta) \boldsymbol{\sigma}^g, \quad (62)$$

where $\boldsymbol{\sigma}^c$ and $\boldsymbol{\sigma}^g$ are the Cauchy stress tensors for the crystalline and amorphous phases, respectively.

The local dissipation rate is written as,

$$\begin{aligned} \mathfrak{D} = & \mathbf{X}_p^c : \dot{\boldsymbol{\varepsilon}}_p^c + \mathbf{X}_p^g : \dot{\boldsymbol{\varepsilon}}_p^g + \mathbf{X}_t : \dot{\boldsymbol{\varepsilon}}_t + \mathbf{X}_\eta \dot{\eta} \geq 0, \\ \mathbf{X}_p^c = & \boldsymbol{\sigma} - h(\eta) \rho_g \frac{\partial \psi_g^e}{\partial \boldsymbol{\varepsilon}_p^c}, \quad \mathbf{X}_p^g = -h(\eta) \rho_g \frac{\partial \psi_g^e}{\partial \boldsymbol{\varepsilon}_p^g}, \\ \mathbf{X}_t = & -h(\eta) \rho_g \frac{\partial \psi_g^e}{\partial \boldsymbol{\varepsilon}_t}, \\ \mathbf{X}_\eta = & - \left[(\rho_g \psi_e^g - \rho_c \psi_e^c) h'(\eta) + \rho_c \frac{\partial \psi^{ch}}{\partial \eta} - \rho_c \nabla \frac{\partial \psi^\nabla}{\partial \nabla \eta} \right. \\ & \left. - h(\eta) J_g \eta (1 - \eta) \dot{\gamma}_t \sinh \frac{\sigma_e}{\sigma_c} \boldsymbol{\sigma}^g : \frac{\mathbf{S}}{\sigma_e} \text{sign}(\dot{\eta}) \right], \end{aligned}$$

where $\rho_g \frac{\partial \psi_g^e}{\partial \boldsymbol{\varepsilon}_p^c} = \boldsymbol{\sigma}^g$ and $\rho_g \frac{\partial \psi_g^e}{\partial \boldsymbol{\varepsilon}_p^g} = \rho_g \frac{\partial \psi_g^e}{\partial \boldsymbol{\varepsilon}_t} = -\boldsymbol{\sigma}^g$. Then, the work-conjugate driving forces are obtained:

$$\begin{aligned} \mathbf{X}_p^c = & (1 - h(\eta)) \boldsymbol{\sigma}^c, \quad \mathbf{X}_p^g = \mathbf{X}_t = h(\eta) \boldsymbol{\sigma}^g, \\ \mathbf{X}_\eta = & (\psi_e^c - J_g \psi_e^g) h'(\eta) - \frac{\partial \psi^{ch}}{\partial \eta} + \nabla \frac{\partial \psi^\nabla}{\partial \nabla \eta} \\ & + h(\eta) J_g \eta (1 - \eta) \dot{\gamma}_t \sinh \frac{\sigma_e}{\sigma_c} \boldsymbol{\sigma}^g : \frac{\mathbf{S}}{\sigma_e} \text{sign}(\dot{\eta}). \end{aligned} \quad (63)$$

The momentum equilibrium equation is derived from the elastic energy as,

$$\nabla \cdot \boldsymbol{\sigma} = 0, \quad (64)$$

where $\boldsymbol{\sigma}$ is the Cauchy stress tensor, defined as Equation 62. Appropriate boundary conditions can be applied depending on the specific scenario.

3.3. Kinetic equations

The evolution of the system is governed by kinetic equations that describe the rates of change of plastic strains, transformation strain, and the phase field variable η . These rates are functions of the work-conjugate thermodynamic forces, ensuring Thermodynamic consistency. The general form of the kinetic equations is expressed as:

$$\dot{\boldsymbol{\epsilon}}_p^c = f_p^c(\mathbf{X}_p^c, \eta), \dot{\boldsymbol{\epsilon}}_p^g = f_p^g(\mathbf{X}_p^g, \eta), \dot{\boldsymbol{\epsilon}}_t = f_t(\mathbf{X}_t, \eta), \dot{\eta} = f_\eta(\mathbf{X}_\eta, \eta). \quad (65)$$

Using the expressions for the thermodynamic forces and the plastic flow rules, the specific kinetic equations for the system are derived:

$$\begin{aligned} \dot{\eta} = M \left[(\psi_e^c - J_g \psi_g^e) h'(\eta) - \frac{\partial \psi^{ch}}{\partial \eta} + \nabla \frac{\partial \psi^\nabla}{\partial \nabla \eta} \right. \\ \left. + h(\eta) J_g \eta (1 - \eta) \dot{\gamma}_t \sinh \frac{\sigma_e}{\sigma_c} \boldsymbol{\sigma}^g : \frac{\mathbf{S}}{\sigma_e} \text{sign}(\dot{\eta}) \right], \end{aligned} \quad (66)$$

$$\dot{\boldsymbol{\epsilon}}_p^c = \sum_{\alpha=1}^N \dot{\gamma}^\alpha \mathbf{m}^\alpha \otimes \mathbf{n}^\alpha, \quad (67)$$

$$\dot{\boldsymbol{\epsilon}}_p^g = \dot{\gamma}_g \sinh \frac{\sigma_e}{\sigma_0} \frac{\mathbf{S}}{\sigma_e}, \quad (68)$$

$$\dot{\boldsymbol{\epsilon}}_t = \dot{\boldsymbol{\epsilon}}_t = \eta (1 - \eta) \dot{\eta} \text{sign}(\dot{\eta}) \dot{\gamma}_t \sinh \frac{\sigma_e}{\sigma_c} \frac{\mathbf{S}}{\sigma_e}, \quad (69)$$

$$\mathbf{n} \cdot \nabla \eta = 0. \quad (70)$$

Equation 66 defines the evolution of the field variable η , governed by the TDGL equation.

Equation 67 describes the plastic deformation in the crystalline phase, where α indicates a slip system, \mathbf{m}^α and \mathbf{n}^α are the slip direction and normal vector to the slip plane, respectively. The shear rate $\dot{\gamma}^\alpha$ on the slip plane reads,

$$\dot{\gamma}^\alpha = \dot{\gamma}_0 \left| \frac{\tau^\alpha}{\tau_c^\alpha} \right|^{\frac{1}{m}} \text{sgn}(\tau^\alpha),$$

where τ^α is the resolved shear stress, τ_c^α is the slip resistance, and m is the strain rate sensitivity.

320 Equation 68 governs the evolution of plastic strain in the amorphous phase, where \mathbf{S} is the deviatoric stress tensor, σ_e is the equivalent Mises stress, σ_0 is the yield stress, and $\dot{\gamma}_g$ is the viscoplastic multiplier.

Equation 69 gives the transformation strain rate during amorphization, where $\dot{\gamma}_t$ is the reference rate of transformation strain, and σ_c is the critical stress for amorphization.

The last Equation 70 is the Neumann boundary condition for the phase field variable η , which ensures stability.

3.4. Non-dimensional linearized equations

Before performing numerical simulations, it is essential to derive dimensionless equations to simplify the computational framework and eliminate unnecessary parameters[41].

330 We define the dimensionless spatial coordinates and time as:

$$\begin{aligned}\tilde{x} &= \frac{x}{l_0}, & \tilde{y} &= \frac{y}{l_0}, & \tilde{z} &= \frac{z}{l_0}, \\ \tilde{t} &= tM\kappa,\end{aligned}$$

where l_0 is the characterized length, κ is the energy barrier coefficient, and M is the mobility of the field variable. The dimensionless Laplace operator is expressed as,

$$\tilde{\nabla}^2 = \frac{\partial^2}{\partial \tilde{x}^2} + \frac{\partial^2}{\partial \tilde{y}^2} + \frac{\partial^2}{\partial \tilde{z}^2}.$$

The dimensionless elastic constants and stress tensors are defined as,

$$\begin{aligned}\tilde{\mathbb{C}}_c &= \frac{\mathbb{C}_c}{\kappa}, & \tilde{\mathbb{C}}_g &= \frac{\mathbb{C}_g}{\kappa}, \\ \tilde{\boldsymbol{\sigma}}^c &= \tilde{\mathbb{C}}_c : \boldsymbol{\varepsilon}_e^c, & \tilde{\boldsymbol{\sigma}}^g &= \tilde{\mathbb{C}}_g : \boldsymbol{\varepsilon}_e^g.\end{aligned}$$

With dimensionless variables, the kinetic equations for the system are rewritten as:

$$\begin{aligned}\frac{\partial \eta}{\partial \tilde{t}} &= (\tilde{\psi}_e^c - J_g \tilde{\psi}_e^g) h'(\eta) - (A\eta - B\eta^2 + C\eta^3) + \tilde{\beta} \tilde{\nabla}^2 \eta \\ &\quad + h(\eta) J_g \eta (1 - \eta) \dot{\gamma}_t \sinh \frac{\sigma_e}{\sigma_c} \tilde{\boldsymbol{\sigma}}^g : \frac{\mathbf{S}}{\sigma_e} \text{sign}(\dot{\eta}), \\ \frac{\partial \boldsymbol{\varepsilon}_p^c}{\partial \tilde{t}} &= \sum_{\alpha=1}^N \dot{\gamma}^\alpha \mathbf{m}^\alpha \otimes \mathbf{n}^\alpha, \\ \frac{\partial \boldsymbol{\varepsilon}_p^g}{\partial \tilde{t}} &= \dot{\gamma}_g \sinh \frac{\sigma_e}{\sigma_0} \frac{\mathbf{S}}{\sigma_e}, \\ \frac{\partial \boldsymbol{\varepsilon}_t}{\partial \tilde{t}} &= \eta(1 - \eta) \dot{\eta} \text{sign}(\dot{\eta}) \dot{\gamma}_t \sinh \frac{\sigma_e}{\sigma_c} \frac{\mathbf{S}}{\sigma_e}, \\ \mathbf{n} \cdot \tilde{\nabla} \eta &= 0,\end{aligned}\tag{71}$$

where $\tilde{\beta} = \frac{\beta}{\kappa l_0^2}$.

The dimensionless equations simplify the computational framework by reducing the number of parameters, making the model more efficient for numerical simulations. By scaling the spatial and temporal variables, the equations retain their physical accuracy while enabling simulations across a wide range of conditions. This approach aligns with the main goal of Section 3, which is to improve computational efficiency without compromising the essential physics of stress-induced amorphization.

Numerical simulations provides insights into the microstructural evolution and stress-driven phase transformations that are challenging to capture experimentally. In this section, we apply the proposed phase-field model to investigate three key phenomena associated with stress-induced amorphization: the formation of amorphous shear bands, the effect of grain size on amorphization, and surface amorphization under compression. These case studies not only validate the model but also offer quantitative predictions and new insights into the mechanisms driving amorphization.

To perform these simulations, we utilize a combination of numerical methods tailored to the dimensionality and complexity of problems. The Euler method is employed for time integration, while the finite difference method is used for two-dimensional simulations. For three-dimensional problems, we adopt the Multiphysics Object-Oriented Simulation Environment (MOOSE) framework [76], which provides an efficient finite element implementation for modeling the amorphization process under compression. Together, these cases enable a comprehensive exploration of stress-induced amorphization across different scenarios.

4.1. Case 1: Amorphous shear band

To investigate the formation of amorphous shear bands, we simulate a 2D square cell of nanocrystalline NiTi alloy with an initial amorphous defect. This defect mimics microstructural imperfections, such as micro-cracks or localized disorder, commonly found in real materials. The simulation domain has a dimensionless length of $\tilde{L} = 64$, and the amorphous defect is initialized as a rectangular region within the crystalline matrix (Figure 3). A pure shear deformation is applied, with periodic boundary conditions on the left and right boundaries and displacement-controlled conditions on the top and bottom boundaries. This setup allows us to observe how the amorphous phase propagates and how shear bands form under deformation.

The material parameters used in the simulation are based on previous studies [12, 14, 41, 68]. Mechanical parameters for the crystalline and amorphous phases of the NiTi alloy include $E_c = 64.3 \text{ GPa}$, $\nu_c = 0.43$, $\dot{\gamma}_0 = 1 \times 10^{-6}$, $m = 3$, $h = 3 \text{ GPa}$, $\tau_{c,0} = 2.7 \text{ GPa}$, $E_g = 47 \text{ GPa}$, $\nu_g = 0.3$, $\dot{\gamma}_t = 5 \times 10^{-3}$, $\sigma_c = 1.2 \text{ GPa}$, $\dot{\gamma}_g = 10^{-6}$, $\sigma_0 = 3.2 \text{ GPa}$. Other key parameters are $\kappa = 4.403 \times 10^7 \text{ J} \cdot \text{m}^{-3}$, $J_g = 1.1$, $\varepsilon_0 = 0.1$, $A = 12$, $B = 30$, and $C = 14$, $\tilde{\beta} = 2$, and $\frac{d\varepsilon_{12}}{dt} = 0.6$. The characterized size l_0 is determined using the interfacial energy density $\gamma = 187 \text{ mJ} \cdot \text{m}^{-2}$, yielding $l_0 = \frac{3\gamma}{4\kappa\sqrt{2\tilde{\beta}}} = 1.6 \text{ nm}$ [41]. The simulation domain is $\tilde{L} \times \tilde{L} = 64 \times 64$, corresponding to a physical size of $L \sim 100 \text{ nm}$.

Figure 4 presents the simulation results for shear deformation. This first row shows the evolution of phase field variable η , and the second one presents changes of the shear stress. Initially,

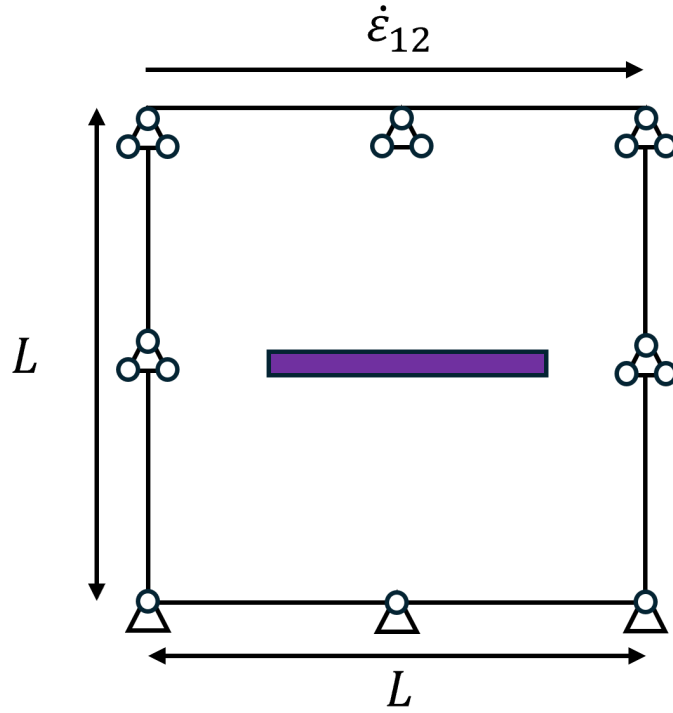


Figure 3: Numerical setup of shear in two dimensions. $\dot{\epsilon}$ is the loading rate. L is the size of the simulation square cell. The purple box gives the initial amorphous defects.

the NiTi alloy contains a localized amorphous defect within the crystalline matrix (Figure 4(a)). Upon applying shear deformation, the shear stress increase, particularly near the amorphous defect, driving the propagation of the amorphous phase along high-stress trajectories (Figure 4(b) and (c)). Eventually, a fully developed amorphous shear band emerges, characterized by highly localized strains (Figure 4(d)).

To further understand the role of deformation in amorphization, we examine the evolution of the elastic strain energy in the small green region (Figure 5(a), same as Figure 4). This region is initialized as the crystalline phase and transforms into the amorphous phase after deformation. Figure 5(b) shows the elastic strain energy stored in the crystalline (blue) and amorphous (red) phases, respectively. Before $\tilde{t} = 5$, the elastic energy stored in the crystalline phase is much smaller than that in the amorphous phase, indicating that the crystalline phase is more stable. Under high stress, the crystalline phase becomes elastically unstable, leading to a rapid decrease in the elastic strain energy of the amorphous phases and an increase in the crystalline phase ($5 < \tilde{t} < 7$). After $\tilde{t} = 7$, the amorphous phase becomes more stable and remain dominant in this region, which is aligned with Figure 4(c) and (d).

The simulation results demonstrate that amorphous shear bands form as a result of stress-driven propagation of the amorphous phase along high-stress trajectories. The presence of initial amor-

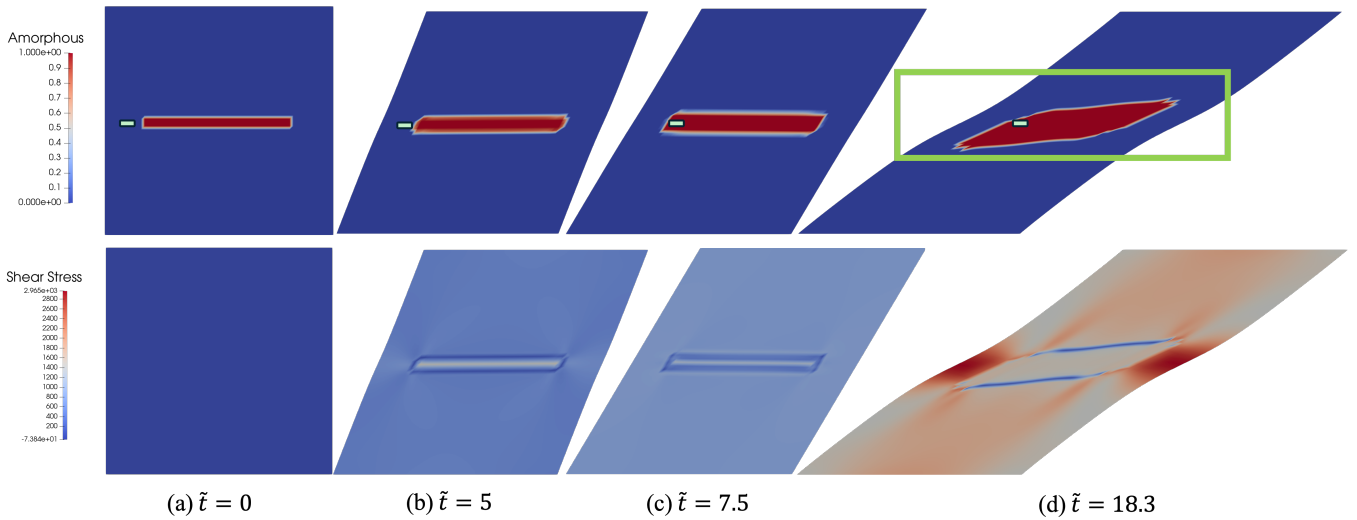


Figure 4: Results of shear deformation in two dimensions. The first row shows the evolution of the amorphous phase, while the second row presents the corresponding shear stress σ_{xy} . The orange box highlights the formation the amorphous shear band. The change of elastic strain energy in the crystalline and amorphous phases of the small green box is compared in the Figure 5.

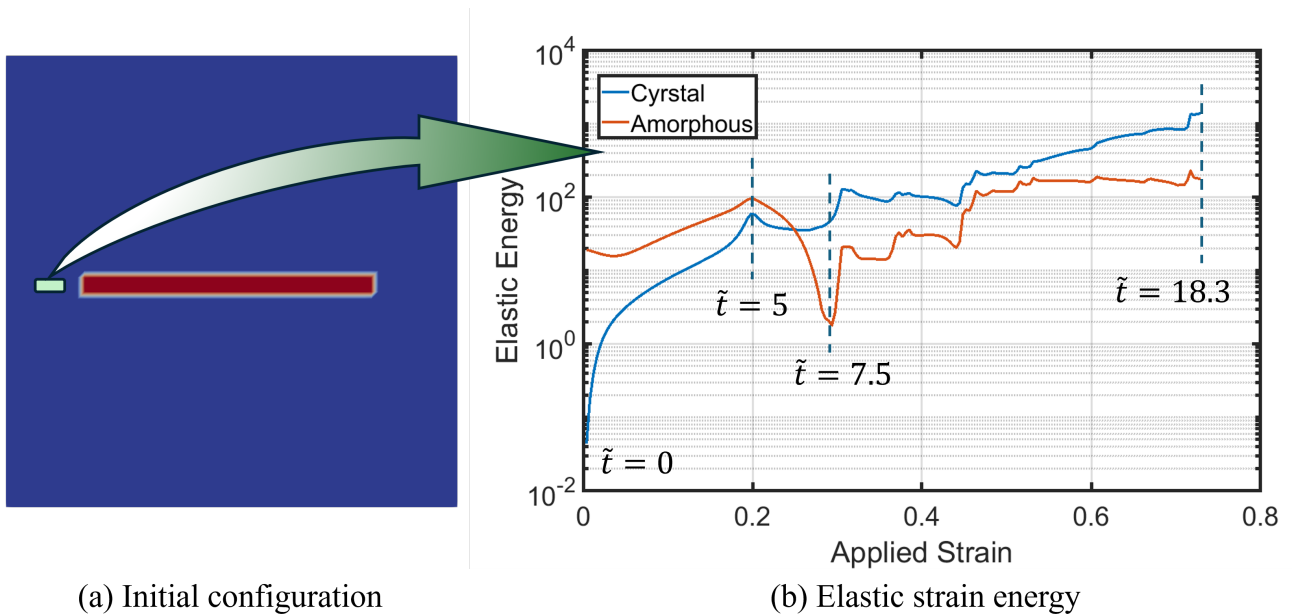


Figure 5: Comparison of the elastic strain energy stored in the crystalline and amorphous phases. (a) The small green box in Figure 4 is chosen for the energy comparison. (b) The elastic energy stored in the crystalline (blue) and amorphous (red) phases, respectively.

phous defects facilitates the nucleation and growth of shear bands, highlighting the critical role of
 390 microstructural imperfections in driving amorphization. Additionally, the energy analysis reveals
 that amorphization serves as an effective mechanism for dissipating energy in highly deformed ma-
 terials, especially when plastic deformation is inhibited due to strain strengthening in the crystalline
 phase.

4.2. Case 2: Grain size effect

In order to investigate the effect of grain size on amorphization, we simulate a multi-grain system
 inspired by Xu et al. [69]. The simulation domain consists of a polycrystalline structure with grain
 size D and a fixed amorphous grain boundary width of $2l$ (Figure 6). To isolate grain size as the sole
 variable, crystallographic anisotropy is neglected, and amorphous grain boundaries are assumed to
 be identical. All material parameters are the same as those used in the previous case.

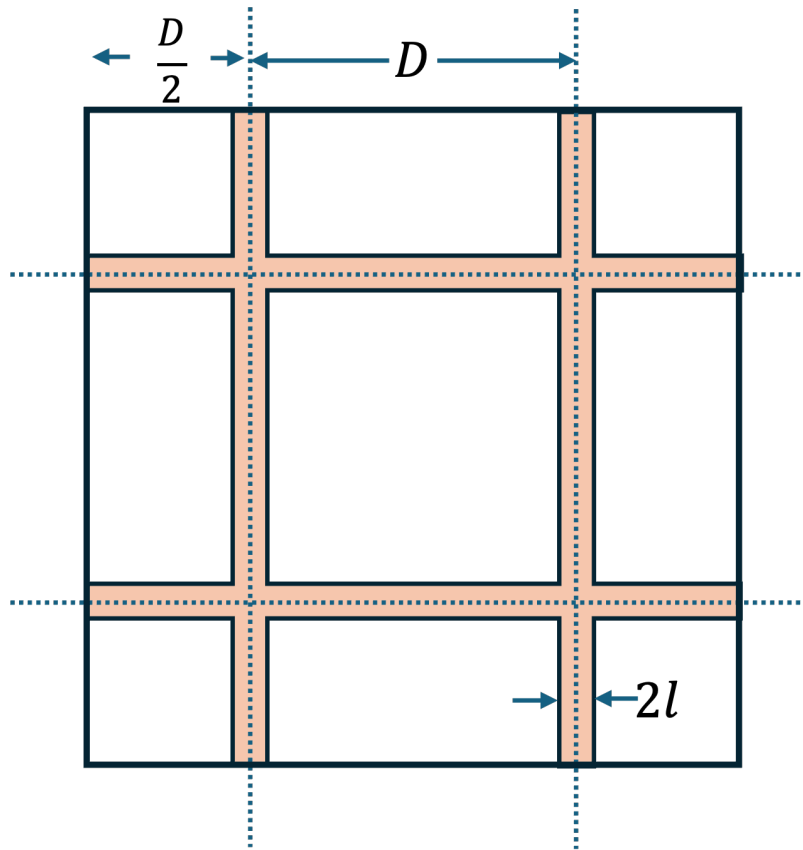


Figure 6: Multi-grain simulation setting. D is the dimensionless size of grains and $2l$ is the dimensionless width of
 amorphous grain boundary, which is fixed.

400 We perform six simulations with grain sizes ranging from $D = 20$ to $D = 70$ and $l = 1$ is chosen.
 Figure 7 shows the evolution of the polycrystalline structure for $D = 30$. The first row illustrates
 the propagation of amorphous grain boundaries, while the second row shows the evolution of the

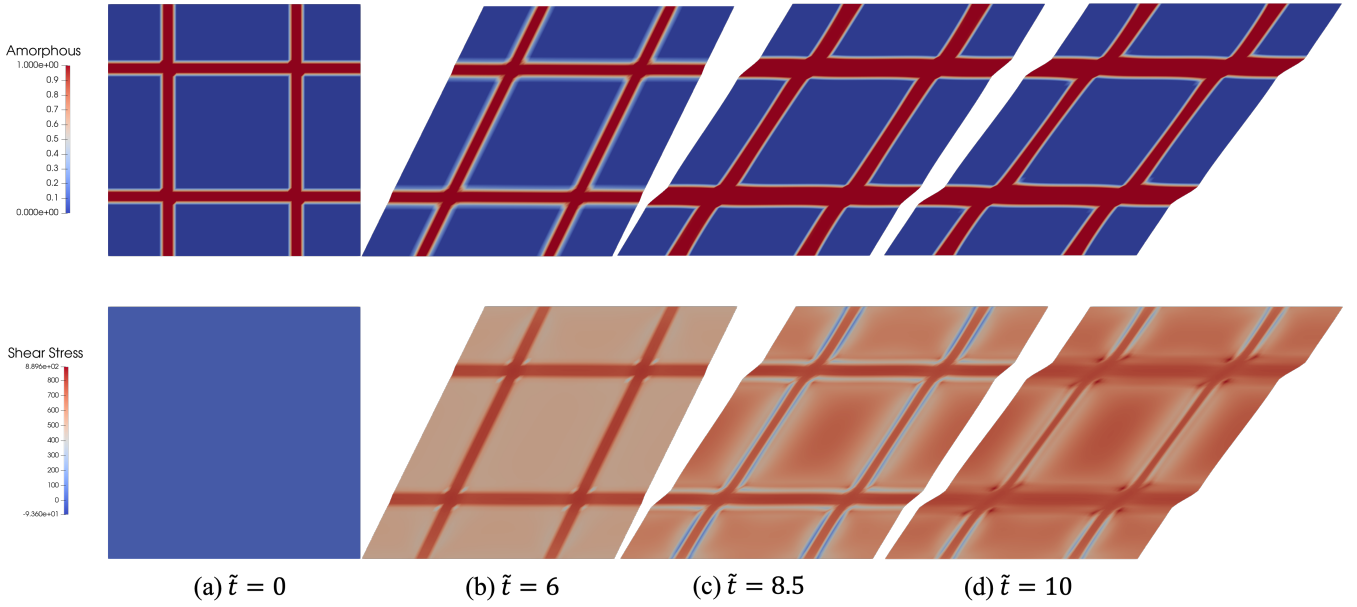


Figure 7: Evolution of the polycrystalline structure for $D = 30$. The first row shows the propagation of amorphous grain boundaries, and the second row presents the evolution of the shear stress σ_{xy} .

shear stress σ_{xy} . As deformation progresses, amorphous phases nucleate and propagate along grain boundaries, leading to the formation of shear bands.

Figure 8 summarizes the grain size effect on amorphization. In Figure 8(a), the volume fraction of amorphous phases (V_g) increases with applied strain. Smaller grains exhibit a higher initial volume fraction of amorphous phases and a more significant increase in V_g during deformation (Figure 8(b), where the increase in volume fraction of amorphous phases is presented). The results indicate that smaller grains facilitate the development of amorphous phases, consistent with experimental findings [15, 24].

The strain-volume fraction curve exhibits horizontal strain jumps connected by nearly vertical volume fraction steps, as shown in Figure 8(a). This avalanche-like behavior, observed numerically for the first time, suggests that amorphization occurs in discrete bursts. During an avalanche, new amorphous phases form rapidly, dissipating energy and reducing the stress for further amorphization. This behavior is analogous to avalanche dynamics commonly observed in plastic deformation, indicating that amorphization may be a critical-like process governed by similar dynamics.

The change in volume fraction of amorphous phases demonstrate that the threshold strain for amorphization increases slightly with grain size. In Figure 8(b), the curves for different grain sizes are close at the beginning, indicating that the stress condition dominates the nucleation of amorphous phases. For larger grains, the reduced number of nucleation sites slightly increases the

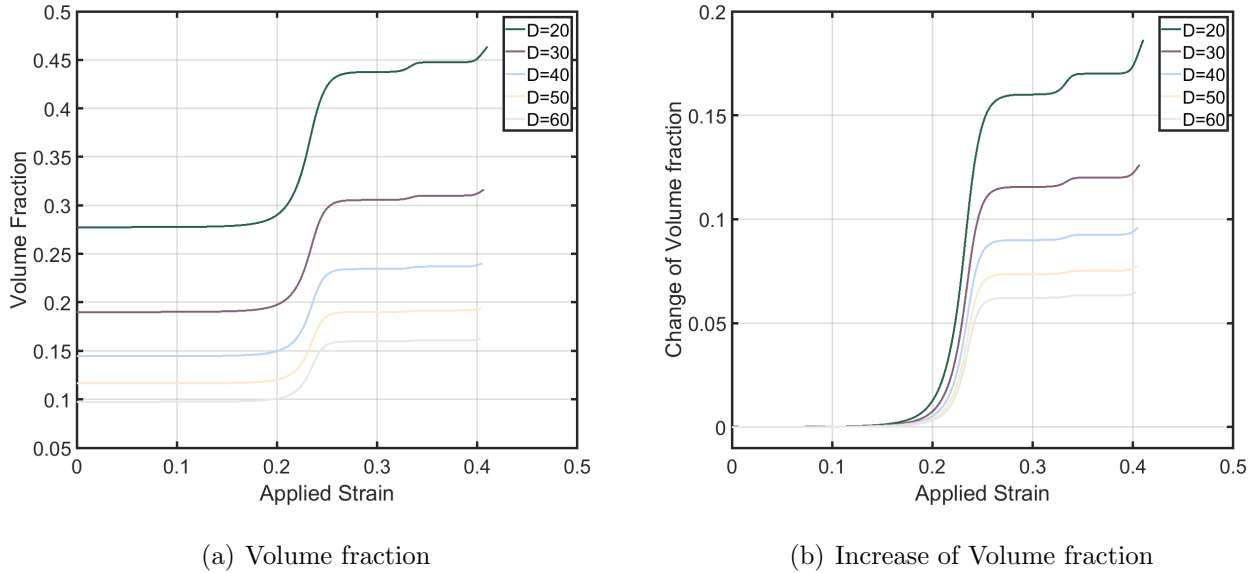


Figure 8: Grain size effect on amorphization. (a) Volume fraction of amorphization (V_g) under large strains. (b) Increase of the volume fraction of amorphous phases ($V_g - V_g^0$), where V_g^0 is the initial volume fraction.

threshold strain, but the change is minimal within the simulated grain size range.

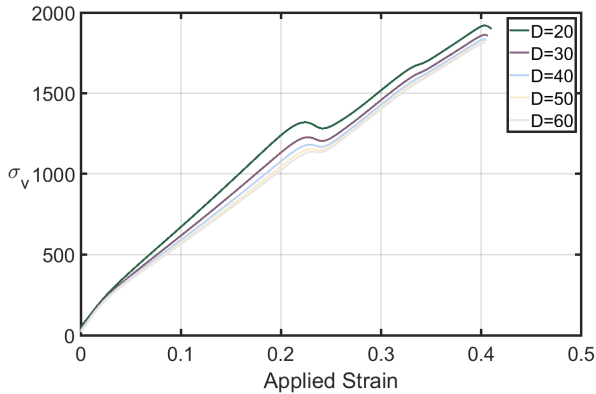
Figure 9 shows the stress-strain curves and yield stress as a linear function of $D^{-1/2}$. The yield stress increases with decreasing grain size, demonstrating the famous Hall-Petch effect. This observation validates the proposed phase-field model, as it captures the Hall-Petch behavior even in the absence of dislocations, highlighting the importance of continuum approaches for studying amorphization.

4.3. Case 3: Surface amorphization

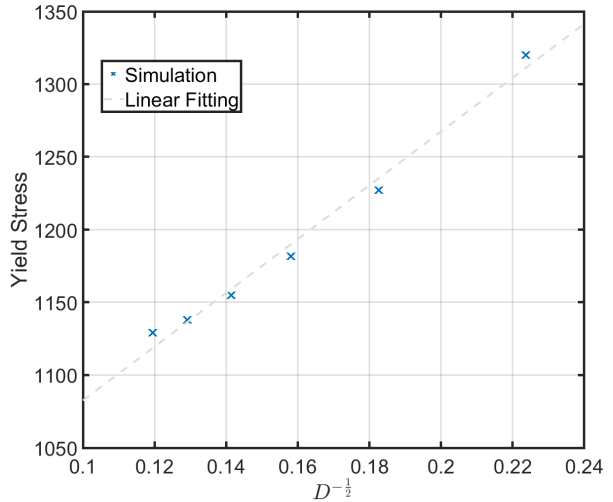
To investigate surface amorphization under compression, we perform 3D simulations using MOOSE [76]. The simulation domain is a cubic cell with a side length of $L = 170$ nm. A random initial value between 0 and 0.1 is assigned to the phase variable η to represent the initial amorphous defects.

Compression is applied along the Z -axis to the nanocrystalline NiTi shape-memory alloy, The simulation parameters are the same as those used in the previous cases.

Figure 10 presents the results of the 3D compression simulation. The first row in Figure 10 illustrates an overview of the amorphous phase distribution (left) and the stress magnitude σ_x (right). The subsequent rows show cross-sectional views along the Y-Z, X-Z, and X-Y planes. The phase variable η highlights the amorphous regions, while $\sigma_x = \sqrt{\sigma_{xx}^2 + \sigma_{xy}^2 + \sigma_{xz}^2}$ represents the stress distribution. The results indicate that amorphous phases nucleate primarily on surfaces and in interior regions under high stress.



(a) Stress v.s. Strain



(b) Yield Stress v.s $D^{-\frac{1}{2}}$

Figure 9: Hall-Petch effect. (a) Stress-strain curves for different grain sizes. (b) Yield stress as a linear function of $D^{-\frac{1}{2}}$. The blue line represents the linear fitting.

440 Figure 11 shows the isosurfaces of $\eta = 0.5$, which is considered as a threshold for amorphization. At lower compression strain ($\varepsilon_c \leq 0.302$), amorphous phases form predominantly on the surfaces (Figure 11(a) and (b)). As the strain increases, the amorphous regions expand and align with the diagonal regions and surfaces of the compressed cell (Figure 11(c) and (d)). These regions correspond to areas of high distortion and are consistent with experimental observations [6, 9, 11].

The results highlight the role of stress in driving amorphization, complementing the findings from the previous cases. While Case 1 demonstrated the formation of amorphous shear bands and Case 2 revealed the grain size dependence of amorphization, this case emphasizes the importance of surface and geometric effects. Together, these insights underscore the versatility of the proposed model in capturing the key mechanisms of stress-induced amorphization and its potential for studying
 450 amorphization as a deformation mechanism in nanocrystalline materials at the mesoscale.

5. Conclusions

This study introduces a novel phase-field model to investigate amorphization under severe plastic deformation. By integrating elastoplastic theory with phase field approaches, the model incorporates a new deviatoric stress-dependent transformation strain tensor, which captures the stress-driven nature of amorphization. This framework couples transformation strain energy with plastic work, enabling the simulation of amorphous phase nucleation and propagation under high stress. The proposed model provides a robust and thermodynamically consistent tool for studying amorphization as a deformation mechanism in nanocrystalline materials.

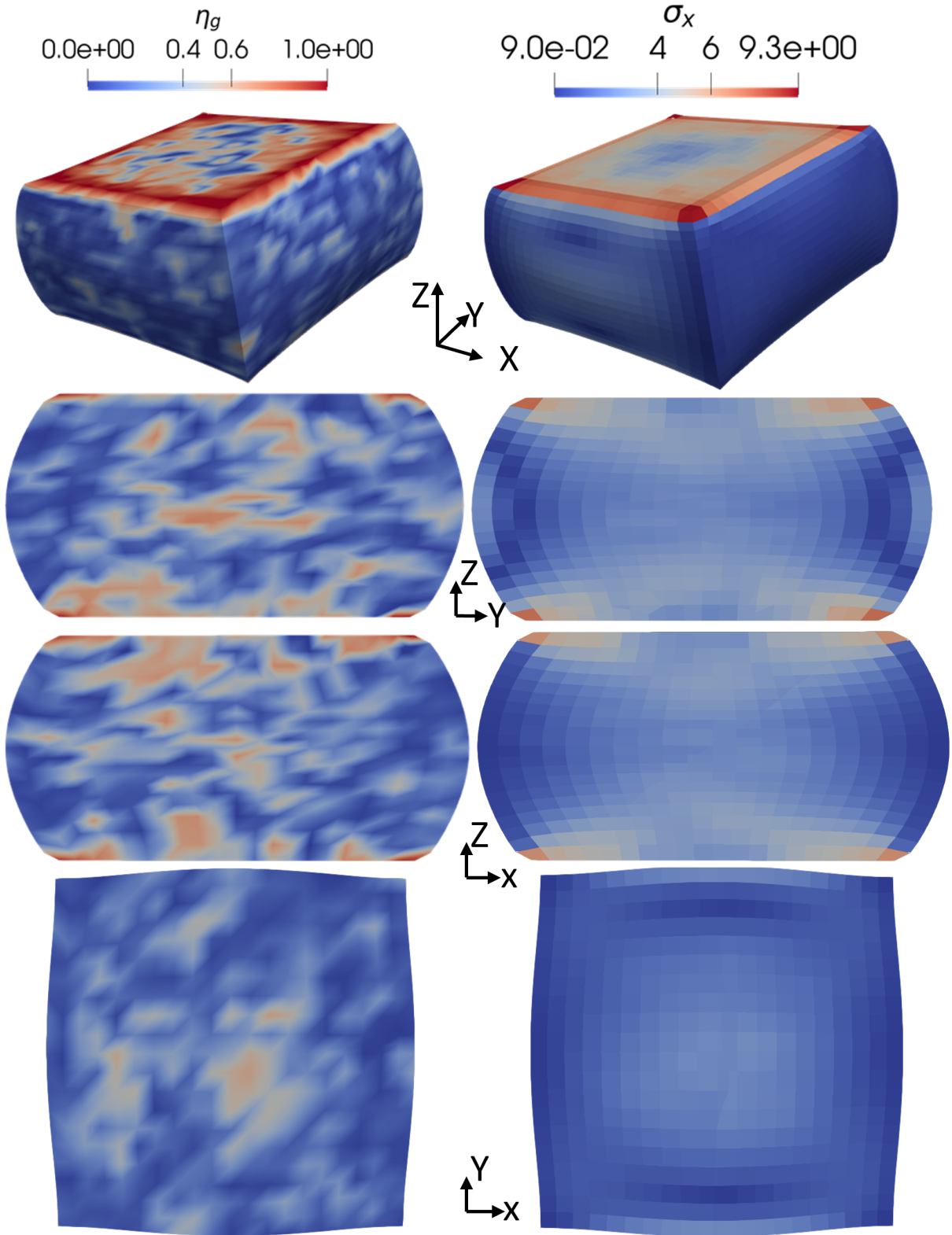


Figure 10: Results of compression in three dimensions. The first row illustrates the distributions of the order parameter η (left), and the stress magnitude σ_x (right). The following rows show the cross-sectional views along the Y-Z, X-Z, and X-Y planes.

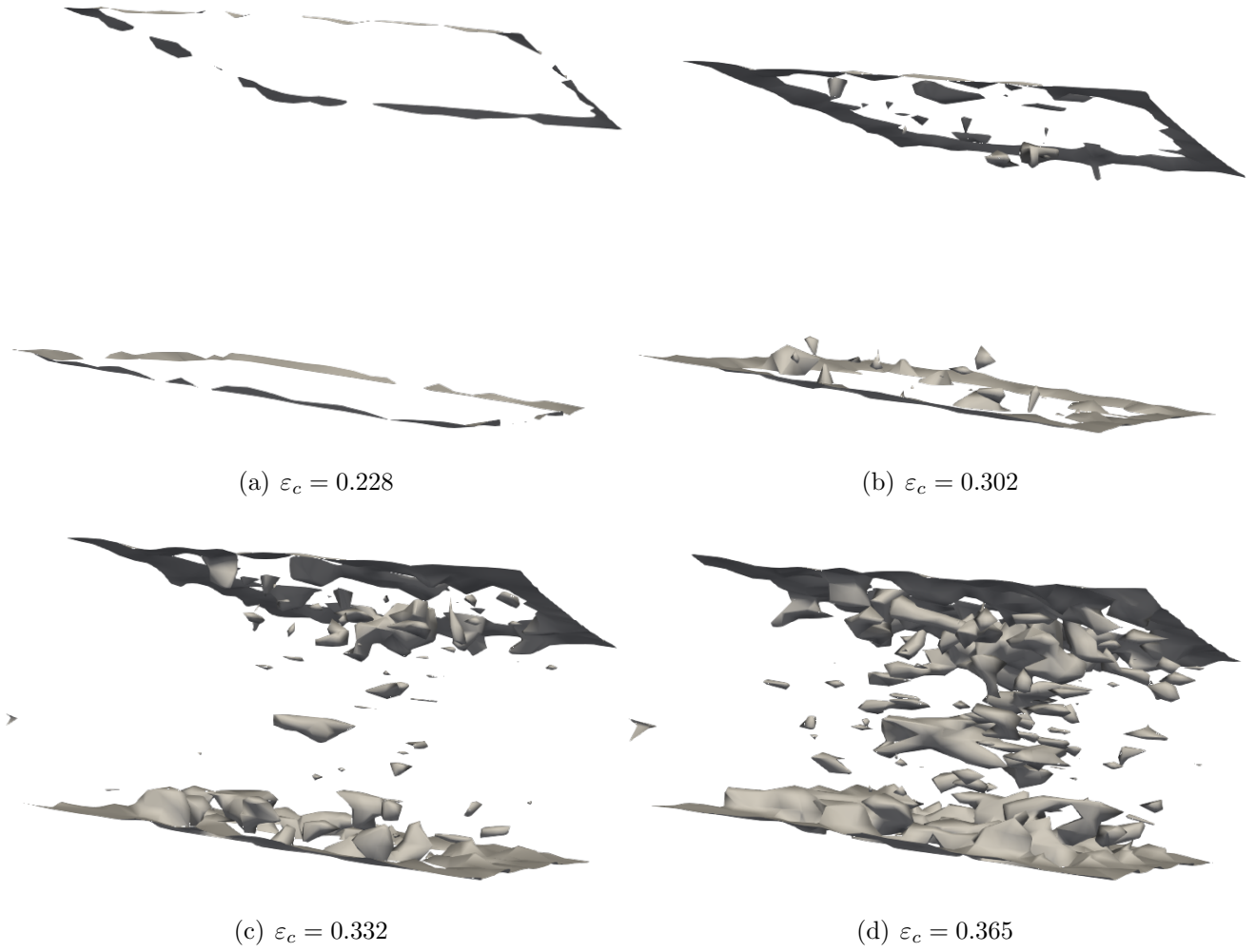


Figure 11: Isosurfaces of $\eta = 0.5$ under compression. (a) and (b) show amorphous phases forming on surfaces at lower strains. (c) and (d) illustrate the expansion of amorphous regions into diagonal and highly distorted areas at higher strains.

The numerical simulations validate the model and provide new insights into stress-induced amor-
460 phization. The formation and propagation of amorphous shear bands, driven by elastic instability
in the crystalline phase, align with experimental observations and highlight the critical role of stress
in driving amorphization. The grain size effect is also captured, demonstrating that smaller grains
facilitate amorphization, while larger grains increase the critical strain required for amorphous phase
formation. This behavior is consistent with the Hall-Petch effect, further validating ability of the
model to reproduce fundamental material behaviors.

A particularly novel discovery is the avalanche-like dynamics of stress-induced amorphization,
characterized by discrete bursts of amorphous phase formation. This critical-like behavior un-
derscores the interplay between amorphization and plasticity, offering a new perspective on the
mechanisms governing deformation in nanocrystalline materials. Additionally, 3D simulations re-
470 veal that amorphous phases nucleate at surfaces and stress concentrators, such as diagonal regions
in compressed cells. These findings are consistent with in situ experimental studies and emphasize
the importance of surface and geometric effects in amorphization.

Together, these results demonstrate the versatility of the proposed model in capturing the key
mechanisms of stress-induced amorphization. By reproducing experimentally observed phenomena,
such as the Hall-Petch effect and surface amorphization, the model provides a quantitative frame-
work for understanding the interplay between stress, defects, and phase transformation. These
insights have significant implications for material design, particularly for developing materials with
enhanced resistance to deformation-induced amorphization under extreme mechanical conditions.

Looking ahead, the model can be extended to include additional deformation mechanisms and
480 defects, such as dislocations and grain boundary evolution, which play a critical role in amorphiza-
tion. Incorporating thermal effects and temperature-dependent material properties will further
enhance applicability of the proposed model. Large-scale simulations and experimental validation
will also be pursued to bridge the gap between mesoscale modeling and macroscale material behav-
ior. This work lays the groundwork for advancing predictive models of amorphization and provides
a powerful tool for studying the underlying mechanisms of deformation-induced amorphization in
crystalline materials.

Acknowledgement

This work was supported by the Hong Kong Research Grants Council Collaborative Research
Fund C6016-20G and the Project of Hetao Shenzhen-HKUST Innovation Cooperation Zone HZQB-
490 KCZYB-2020083.

Appendix: Symbols

Table 1: List of symbols in finite strain framework

Symbol	Meaning
η	Order parameter
V_g	Volume fraction of the amorphous phase
ρ	Mass density of the system
ρ_c/ρ_g	Mass density of the crystalline/amorphous phase
J_g	Mass density ratio between the crystalline and amorphous phase
Ω_0/Ω	Reference/deformed configuration
\boldsymbol{x}	Material point in Ω_0
\boldsymbol{X}	Image point in Ω
\boldsymbol{F}	Total deformation gradient
$\boldsymbol{F}_c/\boldsymbol{F}_g$	Deformation gradient in the crystalline/amorphous phase
$\boldsymbol{F}_e^c/\boldsymbol{F}_e^g$	Elastic deformation gradient in the crystalline/amorphous phase
$\boldsymbol{F}_p^c/\boldsymbol{F}_p^g$	Plastic deformation gradient in the crystalline/amorphous phase
\boldsymbol{F}_t	Transformation gradient
$\boldsymbol{L}_p^c/\boldsymbol{L}_p^g$	Plastic velocity gradient in the crystalline/amorphous phase
N_s	Number of slip systems in crystal
α, β	Indices of slip systems
$\dot{\gamma}^\alpha$	Shear rate on the slip system α
\boldsymbol{m}^α	Slip direction on the slip system α
\boldsymbol{n}^α	Slip normal of the slip system α
τ^α	Resolved stress on the slip system α
$\dot{\gamma}_0$	Reference shear rate
m	Strain rate sensitivity
τ_c^α	Slip resistance on the slip system α
$h_{\alpha\beta}$	Hardening matrix
$\hat{\boldsymbol{\tau}}^g$	Deviatoric second Kirchhoff stress tensor
\boldsymbol{N}	Visco-plastic flow vector
$\dot{\gamma}_g$	Visco-plastic multiplier
\boldsymbol{R}_e	Elastic rotation tensor
A	A material parameter

Symbol	Meaning
τ_{eq}^g	Kirchhoff equivalent stress tensor
τ^*	Reference stress for amorphous phase
$\dot{\gamma}_t$	Reference rate of transformation strain
ψ	Total energy functional density
ψ^{ch}	Local phase separation energy density
ψ^∇	Gradient energy density
ψ_e^c/ψ_e^p	Elastic strain energy density in the crystalline/amorphous phase
A, B, C	Parameters determine local phase separation energy
κ	Energy barrier between the crystalline and amorphous phase
β	Coefficients related to the interfacial energy
$\mathbf{E}_e^c/\mathbf{E}_e^g$	Elastic strain tensor in the crystalline/amorphous phase
$\mathbb{C}_c/\mathbb{C}_g$	Elastic coefficients in the crystalline/amorphous phase
$\mathbf{P}^c/\mathbf{P}^g$	First Piola-Kirchhoff stress tensor in the crystalline/amorphous phase
$\boldsymbol{\sigma}^c/\boldsymbol{\sigma}^g$	Cauchy stress tensor in the crystalline/amorphous phase
$\hat{\boldsymbol{\sigma}}^c/\hat{\boldsymbol{\sigma}}^g$	Second Kirchhoff stress tensor in the crystalline/amorphous phase
\mathbf{P}	First Piola-Kirchhoff stress tensor
$\mathbf{X}_p^c/\mathbf{X}_p^g$	Work-conjugate force for plastic strain in the crystalline/amorphous phase
$\mathbf{X}_t/\mathbf{X}_\eta$	Work-conjugate force for transformation strain and phase field variable
M	Mobilities for amorphization

References

- [1] J. Koike, D. M. Parkin, and M. Nastasi. Crystal-to-amorphous transformation of NiTi induced by cold rolling. *Journal of Materials Research*, 5(7):1414–1418, July 1990. ISSN 0884-2914, 2044-5326. doi: 10.1557/JMR.1990.1414.
- [2] J.Y. Huang, H. Yasuda, and H. Mori. Deformation-induced amorphization in ball-milled silicon. *Philosophical Magazine Letters*, 79(6):305–314, June 1999. ISSN 0950-0839, 1362-3036. doi: 10.1080/095008399177147.
- [3] T. Waitz, V. Kazykhanov, and H.P. Karnthaler. Martensitic phase transformations in nanocryst-

- 500 talline NiTi studied by TEM. *Acta Materialia*, 52(1):137–147, January 2004. ISSN 13596454. doi: 10.1016/j.actamat.2003.08.036.
- [4] K. Tsuchiya, M. Inuzuka, D. Tomus, A. Hosokawa, H. Nakayama, K. Morii, Y. Todaka, and M. Umemoto. Martensitic transformation in nanostructured TiNi shape memory alloy formed via severe plastic deformation. *Materials Science and Engineering: A*, 438–440:643–648, November 2006. ISSN 09215093. doi: 10.1016/j.msea.2006.01.110.
- [5] Shuyong Jiang, Li Hu, Yanqiu Zhang, and Yulong Liang. Nanocrystallization and amorphization of NiTi shape memory alloy under severe plastic deformation based on local canning compression. *Journal of Non-Crystalline Solids*, 367:23–29, May 2013. ISSN 00223093. doi: 10.1016/j.jnoncrysol.2013.01.051.
- 510 [6] S. Zhao, E.N. Hahn, B. Kad, B.A. Remington, C.E. Wehrenberg, E.M. Bringa, and M.A. Meyers. Amorphization and nanocrystallization of silicon under shock compression. *Acta Materialia*, 103:519–533, January 2016. ISSN 13596454. doi: 10.1016/j.actamat.2015.09.022.
- [7] Shuyong Jiang, Zhinan Mao, Yanqiu Zhang, and Li Hu. Mechanisms of nanocrystallization and amorphization of NiTiNb shape memory alloy subjected to severe plastic deformation. *Procedia Engineering*, 207:1493–1498, 2017. ISSN 18777058. doi: 10.1016/j.proeng.2017.10.1086.
- [8] Long Zhang, Haifeng Zhang, Xiaobing Ren, Jürgen Eckert, Yandong Wang, Zhengwang Zhu, Thomas Gemming, and Simon Pauly. Amorphous martensite in β -Ti alloys. *Nature Communications*, 9(1):506, February 2018. ISSN 2041-1723. doi: 10.1038/s41467-018-02961-2.
- [9] Wei Guo, Yifei Meng, Xie Zhang, Vikram Bedekar, Hongbin Bei, Scott Hyde, Qianying Guo, Gregory B. Thompson, Rajiv Shivpuri, Jian-min Zuo, and Jonathan D. Poplawsky. Extremely hard amorphous-crystalline hybrid steel surface produced by deformation induced cementite amorphization. *Acta Materialia*, 152:107–118, June 2018. ISSN 13596454. doi: 10.1016/j.actamat.2018.04.013.
- 520 [10] Xue Kemin, Zhou Yufeng, Tian Wenchun, and Li Ping. Texture evolution and deformation - induced amorphization in high pressure torsion of W. *Materials Today Communications*, 24: 101178, September 2020. ISSN 23524928. doi: 10.1016/j.mtcomm.2020.101178.
- [11] Shiteng Zhao, Zezhou Li, Chaoyi Zhu, Wen Yang, Zhouran Zhang, David E. J. Armstrong, Patrick S. Grant, Robert O. Ritchie, and Marc A. Meyers. Amorphization in extreme deforma-

tion of the CrMnFeCoNi high-entropy alloy. *Science Advances*, 7(5):eabb3108, January 2021. ISSN 2375-2548. doi: 10.1126/sciadv.abb3108.

530

- [12] S. Zhao, B. Li, B.A. Remington, C.E. Wehrenberg, H.S. Park, E.N. Hahn, and M.A. Meyers. Directional amorphization of covalently-bonded solids: A generalized deformation mechanism in extreme loading. *Materials Today*, 49:59–67, October 2021. ISSN 13697021. doi: 10.1016/j.mattod.2021.04.017.
- [13] Peng Hua, Minglu Xia, Yusuke Onuki, and Qingping Sun. Nanocomposite NiTi shape memory alloy with high strength and fatigue resistance. *Nature Nanotechnology*, 16(4):409–413, April 2021. ISSN 1748-3387, 1748-3395. doi: 10.1038/s41565-020-00837-5.
- [14] B.Y. Li, A.C. Li, S. Zhao, and M.A. Meyers. Amorphization by mechanical deformation. *Materials Science and Engineering: R: Reports*, 149:100673, June 2022. ISSN 0927796X. doi: 10.1016/j.mser.2022.100673.
- 540
- [15] Peng Hua, Bing Wang, Chao Yu, Yilong Han, and Qingping Sun. Shear-induced amorphization in nanocrystalline NiTi micropillars under large plastic deformation. *Acta Materialia*, 241:118358, December 2022. ISSN 13596454. doi: 10.1016/j.actamat.2022.118358.
- [16] Ilya A. Ovid’ko. Nanoscale amorphization as a special deformation mode in nanowires. *Scripta Materialia*, 66:402–405, 2012. URL <https://api.semanticscholar.org/CorpusID:137151211>.
- [17] Hosni Idrissi, Philippe Carrez, and Patrick Cordier. On amorphization as a deformation mechanism under high stresses. *Current Opinion in Solid State and Materials Science*, 26(1):100976, February 2022. ISSN 13590286. doi: 10.1016/j.cossms.2021.100976.
- 550
- [18] Hosni Idrissi, Armand Béché, Nicolas Gauquelin, Ihtasham Ul-Haq, Caroline Bollinger, Sylvie Demouchy, Johan Verbeeck, Thomas Pardoën, Dominique Schryvers, and Patrick Cordier. On the formation mechanisms of intragranular shear bands in olivine by stress-induced amorphization. *Acta Materialia*, 239:118247, October 2022. ISSN 13596454. doi: 10.1016/j.actamat.2022.118247.
- [19] Shiteng Zhao and Xiaolei Wu. Amorphization-mediated plasticity. *Nature Materials*, 22(9):1057–1058, September 2023. ISSN 1476-1122, 1476-4660. doi: 10.1038/s41563-023-01638-6.

- [20] Jun-ichi Koike, D. M. Parkin, and M. Nastasi. The role of shear instability in amorphization of cold-rolled NiTi. *Philosophical Magazine Letters*, 62(4):257–264, October 1990. ISSN 0950-0839, 1362-3036. doi: 10.1080/09500839008215132.
- 560 [21] Eita Tochigi, Eita Tochigi, Eita Tochigi, Eloisa Zepeda-Alarcon, H. R. Wenk, A. M. Minor, and A. M. Minor. In situ tem observations of plastic deformation in quartz crystals. *Physics and Chemistry of Minerals*, 41:757–765, 2014. URL <https://api.semanticscholar.org/CorpusID:58889465>.
- [22] Sergey Prokoshkin, Sergey Dubinskiy, Andrey Korotitskiy, Anton Konopatsky, Vadim Sheremetyev, Igor Shchetinin, Alexander Glezer, and Vladimir Brailovski. Nanostructure features and stress-induced transformation mechanisms in extremely fine-grained titanium nickelide. *Journal of Alloys and Compounds*, 779:667–685, March 2019. ISSN 09258388. doi: 10.1016/j.jallcom.2018.11.180.
- 570 [23] Kenjiro Yamada and Carl C. Koch. The influence of mill energy and temperature on the structure of the TiNi intermetallic after mechanical attrition. *Journal of Materials Research*, 8(6):1317–1326, June 1993. ISSN 0884-2914, 2044-5326. doi: 10.1557/JMR.1993.1317. URL <http://link.springer.com/10.1557/JMR.1993.1317>.
- [24] Jinjun Fan, Jia Li, Zaiwang Huang, P.H. Wen, and C.G. Bailey. Grain size effects on indentation-induced plastic deformation and amorphization process of polycrystalline silicon. *Computational Materials Science*, 144:113–119, March 2018. ISSN 09270256. doi: 10.1016/j.commatsci.2017.12.017.
- [25] Valery I. Levitas. Thermomechanical theory of martensitic phase transformations in inelastic materials. *International Journal of Solids and Structures*, 35(9-10):889–940, March 1998. ISSN 00207683. doi: 10.1016/S0020-7683(97)00089-9.
- 580 [26] A. Artemev, Y. Jin, and A.G. Khachaturyan. Three-dimensional phase field model of proper martensitic transformation. *Acta Materialia*, 49(7):1165–1177, April 2001. ISSN 13596454. doi: 10.1016/S1359-6454(01)00021-0.
- [27] A. Yamanaka, T. Takaki, and Y. Tomita. Elastoplastic phase-field simulation of self- and plastic accommodations in Cubic \rightarrow tetragonal martensitic transformation. *Materials Science and Engineering: A*, 491(1-2):378–384, September 2008. ISSN 09215093. doi: 10.1016/j.msea.2008.02.035.

- [28] Alphonse Finel, Y. Le Bouar, A. Gaubert, and U. Salman. Phase field methods: Microstructures, mechanical properties and complexity. *Comptes Rendus. Physique*, 11(3-4):245–256, April 2010. ISSN 1878-1535. doi: 10.1016/j.crhy.2010.07.014.
- 590 [29] Valery I. Levitas, Dong-Wook Lee, and Dean L. Preston. Interface propagation and microstructure evolution in phase field models of stress-induced martensitic phase transformations. *International Journal of Plasticity*, 26(3):395–422, March 2010. ISSN 07496419. doi: 10.1016/j.ijplas.2009.08.003.
- [30] Akinori Yamanaka, Tomohiro Takaki, and Yoshihiro Tomita. Elastoplastic phase-field simulation of martensitic transformation with plastic deformation in polycrystal. *International Journal of Mechanical Sciences*, 52(2):245–250, February 2010. ISSN 00207403. doi: 10.1016/j.ijmecsci.2009.09.020.
- [31] J.D. Clayton and J. Knap. A phase field model of deformation twinning: Nonlinear theory and numerical simulations. *Physica D: Nonlinear Phenomena*, 240(9-10):841–858, April 2011. 600 ISSN 01672789. doi: 10.1016/j.physd.2010.12.012.
- [32] Tae Wook Heo, Yi Wang, Saswata Bhattacharya, Xin Sun, Shenyang Hu, and Long-Qing Chen. A phase-field model for deformation twinning. *Philosophical Magazine Letters*, 91(2):110–121, February 2011. ISSN 0950-0839, 1362-3036. doi: 10.1080/09500839.2010.537284.
- [33] J. Kundin, D. Raabe, and H. Emmerich. A phase-field model for incoherent martensitic transformations including plastic accommodation processes in the austenite. *Journal of the Mechanics and Physics of Solids*, 59(10):2082–2102, October 2011. ISSN 00225096. doi: 10.1016/j.jmps.2011.07.001.
- [34] Hemantha Kumar Yeddu, Amer Malik, John Ågren, Gustav Amberg, and Annika Borgenstam. Three-dimensional phase-field modeling of martensitic microstructure evolution in steels. *Acta Materialia*, 60(4):1538–1547, February 2012. ISSN 13596454. doi: 10.1016/j.actamat.2011.11. 610 039.
- [35] Vladimir A. Levin, Valery I. Levitas, Konstantin M. Zingerman, and Eugene I. Freiman. Phase-field simulation of stress-induced martensitic phase transformations at large strains. *International Journal of Solids and Structures*, 50(19):2914–2928, September 2013. ISSN 00207683. doi: 10.1016/j.ijsolstr.2013.05.003.

- [36] Valery I. Levitas, Arunabha M. Roy, and Dean L. Preston. Multiple twinning and variant-variant transformations in martensite: Phase-field approach. *Physical Review B*, 88(5):054113, August 2013. ISSN 1098-0121, 1550-235X. doi: 10.1103/PhysRevB.88.054113.
- [37] Hui She, Yulan Liu, Biao Wang, and Decai Ma. Finite element simulation of phase field model for nanoscale martensitic transformation. *Computational Mechanics*, 52(4):949–958, October 2013. ISSN 0178-7675, 1432-0924. doi: 10.1007/s00466-013-0856-5.
- [38] Hemantha Kumar Yeddu, Turab Lookman, and Avadh Saxena. Strain-induced martensitic transformation in stainless steels: A three-dimensional phase-field study. *Acta Materialia*, 61(18):6972–6982, October 2013. ISSN 13596454. doi: 10.1016/j.actamat.2013.08.011.
- [39] Amer Malik, Gustav Amberg, Annika Borgenstam, and John Ågren. Effect of external loading on the martensitic transformation – A phase field study. *Acta Materialia*, 61(20):7868–7880, December 2013. ISSN 13596454. doi: 10.1016/j.actamat.2013.09.025.
- [40] R. Schmitt, C. Kuhn, R. Müller, and K. Bhattacharya. Crystal plasticity and martensitic transformations: A phase field approach. *Technische Mechanik - European Journal of Engineering Mechanics*, 34(1):23–38, Jun. 2019. doi: 10.24352/UB.OVGU-2017-051. URL <https://journals.ub.ovgu.de/index.php/techmech/article/view/647>.
- [41] Yuan Zhong and Ting Zhu. Phase-field modeling of martensitic microstructure in NiTi shape memory alloys. *Acta Materialia*, 75:337–347, August 2014. ISSN 13596454. doi: 10.1016/j.actamat.2014.04.013.
- [42] Valery I. Levitas and Mahdi Javanbakht. Interaction between phase transformations and dislocations at the nanoscale. Part 1. General phase field approach. *Journal of the Mechanics and Physics of Solids*, 82:287–319, September 2015. ISSN 00225096. doi: 10.1016/j.jmps.2015.05.005.
- [43] Mahdi Javanbakht and Valery I. Levitas. Interaction between phase transformations and dislocations at the nanoscale. Part 2: Phase field simulation examples. *Journal of the Mechanics and Physics of Solids*, 82:164–185, September 2015. ISSN 00225096. doi: 10.1016/j.jmps.2015.05.006.
- [44] A. Vattré and C. Denoual. Polymorphism of iron at high pressure: A 3D phase-field model for displacive transitions with finite elastoplastic deformations. *Journal of the Mechanics and Physics of Solids*, 92:1–27, July 2016. ISSN 00225096. doi: 10.1016/j.jmps.2016.01.016.

- [45] Simon Schmidt, Wolfgang Dornisch, and Ralf Müller. A phase field model for martensitic transformation coupled with the heat equation. *GAMM-Mitteilungen*, 40(2):138–153, December 2017. ISSN 0936-7195, 1522-2608. doi: 10.1002/gamm.201720005.
- [46] C. Liu, P. Shanthraj, M. Diehl, F. Roters, S. Dong, J. Dong, W. Ding, and D. Raabe. An integrated crystal plasticity–phase field model for spatially resolved twin nucleation, propagation, and growth in hexagonal materials. *International Journal of Plasticity*, 106:203–227, July 2018. ISSN 07496419. doi: 10.1016/j.ijplas.2018.03.009.
- [47] Sam Mirzakhani and Mahdi Javanbakht. Phase field-elasticity analysis of austenite–martensite phase transformation at the nanoscale: Finite element modeling. *Computational Materials Science*, 154:41–52, November 2018. ISSN 09270256. doi: 10.1016/j.commatsci.2018.07.034.
- [48] Xi Xie, Guozheng Kang, Qianhua Kan, Chao Yu, and Qi Peng. Phase field modeling for cyclic phase transition of NiTi shape memory alloy single crystal with super-elasticity. *Computational Materials Science*, 143:212–224, February 2018. ISSN 09270256. doi: 10.1016/j.commatsci.2017.11.017.
- [49] Anup Basak and Valery I. Levitas. Finite element procedure and simulations for a multiphase phase field approach to martensitic phase transformations at large strains and with interfacial stresses. *Computer Methods in Applied Mechanics and Engineering*, 343:368–406, January 2019. ISSN 00457825. doi: 10.1016/j.cma.2018.08.006.
- [50] Fan Peng, Wei Huang, Zhi-Qian Zhang, Tian Fu Guo, and Yu.E. Ma. Phase field simulation for fracture behavior of hyperelastic material at large deformation based on edge-based smoothed finite element method. *Engineering Fracture Mechanics*, 238:107233, October 2020. ISSN 00137944. doi: 10.1016/j.engfracmech.2020.107233.
- [51] Bo Xu, Guozheng Kang, Qianhua Kan, Chao Yu, and Xi Xie. Phase field simulation on the cyclic degeneration of one-way shape memory effect of NiTi shape memory alloy single crystal. *International Journal of Mechanical Sciences*, 168:105303, February 2020. ISSN 00207403. doi: 10.1016/j.ijmecsci.2019.105303.
- [52] Bo Xu and Guozheng Kang. Phase field simulation on the super-elasticity, elastocaloric and shape memory effect of geometrically graded nano-polycrystalline NiTi shape memory alloys. *International Journal of Mechanical Sciences*, 201:106462, July 2021. ISSN 00207403. doi: 10.1016/j.ijmecsci.2021.106462.

- [53] Valery I. Levitas. Phase transformations, fracture, and other structural changes in inelastic materials. *International Journal of Plasticity*, 140:102914, May 2021. ISSN 07496419. doi: 10.1016/j.ijplas.2020.102914.
- [54] Ran Ma and WaiChing Sun. Phase field modeling of coupled crystal plasticity and deformation twinning in polycrystals with monolithic and splitting solvers. *International Journal for Numerical Methods in Engineering*, 122(4):1167–1189, February 2021. ISSN 0029-5981, 1097-0207. doi: 10.1002/nme.6577.
- [55] Anup Basak and Valery I. Levitas. A multiphase phase-field study of three-dimensional martensitic twinned microstructures at large strains. *Continuum Mechanics and Thermodynamics*, 35(4):1595–1624, July 2023. ISSN 0935-1175, 1432-0959. doi: 10.1007/s00161-022-01177-6.
- [56] Songlin Yao, Jidong Yu, Xiaoyang Pei, Yinan Cui, Hao Zhang, Hui Peng, Yi Li, and Qiang Wu. A coupled phase-field and crystal plasticity model for understanding shock-induced phase transition of iron. *International Journal of Plasticity*, 173:103860, February 2024. ISSN 07496419. doi: 10.1016/j.ijplas.2023.103860.
- [57] D. Clayton John. Phase field theory and analysis of pressure-shear induced amorphization and failure in boron carbide ceramic. *AIMS Materials Science*, 1:143–158, 2014. ISSN 2372-0484. doi: 10.3934/matensci.2014.3.143. URL <https://www.aimspress.com/article/doi/10.3934/matensci.2014.3.143>.
- [58] Wen Xi, Xiaoqing Song, Shi Hu, and Zheng Chen. Phase field crystal simulation of stress induced localized solid-state amorphization in nanocrystalline materials. *Journal of Physics: Condensed Matter*, 29(47):475902, November 2017. ISSN 0953-8984, 1361-648X. doi: 10.1088/1361-648X/aa8fee.
- [59] J.D. Clayton, R.B. Leavy, and J. Knap. Phase field modeling of heterogeneous microcrystalline ceramics. *International Journal of Solids and Structures*, 166:183–196, July 2019. ISSN 00207683. doi: 10.1016/j.ijsolstr.2019.02.016.
- [60] Matteo Arricca, Nicoletta Inverardi, Stefano Pandini, Maurizio Toselli, Massimo Messori, and Giulia Scalet. Finite strain continuum phenomenological model describing the shape-memory effects in multi-phase semi-crystalline networks. *Journal of the Mechanics and Physics of Solids*, 195:105955, February 2025. ISSN 00225096. doi: 10.1016/j.jmps.2024.105955.

- [61] Valery I. Levitas. Phase-field theory for martensitic phase transformations at large strains. *International Journal of Plasticity*, 49:85–118, October 2013. ISSN 07496419. doi: 10.1016/j.ijplas.2013.03.002.
- [62] Wei Hong and Xiao Wang. A phase-field model for systems with coupled large deformation and mass transport. *Journal of the Mechanics and Physics of Solids*, 61(6):1281–1294, June 710 2013. ISSN 00225096. doi: 10.1016/j.jmps.2013.03.001.
- [63] Efim Borukhovich, Philipp S. Engels, Jörn Mosler, Oleg Shchyglo, and Ingo Steinbach. Large deformation framework for phase-field simulations at the mesoscale. *Computational Materials Science*, 108:367–373, October 2015. ISSN 09270256. doi: 10.1016/j.commatsci.2015.06.021.
- [64] Daniel Schneider, Felix Schwab, Ephraim Schoof, Andreas Reiter, Christoph Herrmann, Michael Selzer, Thomas Böhlke, and Britta Nestler. On the stress calculation within phase-field approaches: A model for finite deformations. *Computational Mechanics*, 60(2):203–217, August 2017. ISSN 0178-7675, 1432-0924. doi: 10.1007/s00466-017-1401-8.
- [65] Valery I. Levitas and Kamran Samani. Coherent solid/liquid interface with stress relaxation in a phase-field approach to the melting/solidification transition. *Physical Review B*, 84(14): 720 140103, October 2011. ISSN 1098-0121, 1550-235X. doi: 10.1103/PhysRevB.84.140103.
- [66] Y F Gao. An implicit finite element method for simulating inhomogeneous deformation and shear bands of amorphous alloys based on the free-volume model. *Modelling and Simulation in Materials Science and Engineering*, 14(8):1329–1345, December 2006. ISSN 0965-0393, 1361-651X. doi: 10.1088/0965-0393/14/8/004.
- [67] E. V. Tat’yanin, N. F. Borovikov, V. G. Kurdyumov, and V. L. Indenbom. Amorphous shear bands in deformed TiNi alloy. *Physics of the Solid State*, 39(7):1097–1099, July 1997. ISSN 1063-7834, 1090-6460. doi: 10.1134/1.1130038.
- [68] C Schuh, T Hufnagel, and U Ramamurty. Mechanical behavior of amorphous alloys. *Acta Materialia*, 55(12):4067–4109, July 2007. ISSN 13596454. doi: 10.1016/j.actamat.2007.01.052.
- [69] Zhibin Xu, Mengmeng Li, Huijun Zhang, and Yilong Han. Generalization of the Hall-Petch and inverse Hall-Petch behaviors by tuning amorphous regions in 2D solids. *National Science Open*, 2(3):20220058, March 2023. ISSN 2097-1168. doi: 10.1360/nso/20220058.
- [70] Christian Miehe and Jörg Schröder. A comparative study of stress update algorithms for rate-independent and rate-dependent crystal plasticity. *International Journal for Numerical*

Methods in Engineering, 50(2):273–298, January 2001. ISSN 0029-5981, 1097-0207. doi: 10.1002/1097-0207(20010120)50:2<273::AID-NME17>3.0.CO;2-Q.

[71] F. Roters, P. Eisenlohr, L. Hantcherli, D.D. Tjahjanto, T.R. Bieler, and D. Raabe. Overview of constitutive laws, kinematics, homogenization and multiscale methods in crystal plasticity finite-element modeling: Theory, experiments, applications. *Acta Materialia*, 58(4):1152–1211, February 2010. ISSN 13596454. doi: 10.1016/j.actamat.2009.10.058.

[72] Michael E. Kassner, Kamia Smith, and Veronica Eliasson. Creep in amorphous metals. *Journal of Materials Research and Technology*, 4(1):100–107, January 2015. ISSN 22387854. doi: 10.1016/j.jmrt.2014.11.003.

[73] Bernardo P. Ferreira, A. Francisca Carvalho Alves, and F.M. Andrade Pires. An efficient finite strain constitutive model for amorphous thermoplastics: Fully implicit computational implementation and optimization-based parameter calibration. *Computers & Structures*, 281:107007, June 2023. ISSN 00457949. doi: 10.1016/j.compstruc.2023.107007.

[74] Daniel Vallicotti, Ashish Sridhar, and Marc-Andre Keip. VARIATIONALLY CONSISTENT COMPUTATIONAL HOMOGENIZATION OF MICRO-ELECTRO-MECHANICS AT FINITE DEFORMATIONS. *International Journal for Multiscale Computational Engineering*, 16(4):377–395, 2018. ISSN 1543-1649. doi: 10.1615/IntJMCompEng.2018026858.

[75] Valery I. Levitas. Recent *In Situ* Experimental and Theoretical Advances in Severe Plastic Deformations, Strain-Induced Phase Transformations, and Microstructure Evolution under High Pressure. *MATERIALS TRANSACTIONS*, 64(8):1866–1878, August 2023. ISSN 1345-9678, 1347-5320. doi: 10.2320/matertrans.MT-MF2022055.

[76] Alexander D. Lindsay, Derek R. Gaston, Cody J. Permann, Jason M. Miller, David Andrš, Andrew E. Slaughter, Fande Kong, Joshua Hansel, Robert W. Carlsen, Casey Icenhour, Logan Harbour, Guillaume L. Giudicelli, Roy H. Stogner, Peter German, Jacob Badger, Sudipta Biswas, Leora Chapuis, Christopher Green, Jason Hales, Tianchen Hu, Wen Jiang, Yeon Sang Jung, Christopher Matthews, Yinbin Miao, April Novak, John W. Peterson, Zachary M. Prince, Andrea Rovinelli, Sebastian Schunert, Daniel Schwen, Benjamin W. Spencer, Swetha Veeraraghavan, Antonio Recuero, Dewen Yushu, Yaqi Wang, Andy Wilkins, and Christopher Wong. 2.0 - MOOSE: Enabling massively parallel multiphysics simulation. *SoftwareX*, 20:101202, 2022. ISSN 2352-7110. doi: <https://doi.org/10.1016/j.softx.2022.101202>. URL <https://www.sciencedirect.com/science/article/pii/S2352711022001200>.